Ore Geology Reviews 109 (2019) 545–563

Contents lists available at ScienceDirect

Ore Geology Reviews

journal homepage: www.elsevier.com/locate/oregeorev

The nature and partitioning of invisible gold in the pyrite-fluid system

Gleb S. Pokrovski[a,*], Maria A. Kokh[a], Olivier Proux[b], Jean-Louis Hazemann[c], Elena F. Bazarkina[c,f], Denis Testemale[c], Céline Escoda[a,d], Marie-Christine Boiron[e], Marc Blanchard[a], Thierry Aigouy[a], Sophie Gouy[a], Philippe de Parseval[a], Michel Thibaut[a]

[a] Groupe Métallogénie Expérimentale, Géosciences Environnement Toulouse (GET), UMR 5563, Observatoire Midi-Pyrénées, Université de Toulouse, Centre National de la Recherche Scientifique (CNRS), Institut de Recherche pour le Développement (IRD), 14 Avenue Edouard Belin, F-31400 Toulouse, France
[b] Observatoire des Sciences de l'Univers de Grenoble (OSUG), UMS 832 CNRS – Université Grenoble Alpes, 414 rue de la Piscine, F-38400 Saint Martin d'Hères, France
[c] Univ. Grenoble Alpes, CNRS, Institut Néel, 25 Avenue des Martyrs, F-38042 Grenoble Cedex 9, France
[d] Ecole Normale Supérieure Géologie, ENSG, 2 rue du Doyen Marcel Roubault, BP 10162, F-54505 Vandœuvre-lès-Nancy Cedex, Nancy, France
[e] GeoRessources, Université de Lorraine, CNRS, BP 239, F-54506 Vandoeuvre-lès-Nancy, France
[f] Institute of Geology of Ore Deposits, Petrography, Mineralogy and Geochemistry, Russian Academy of Sciences (IGEM RAS), 35 Staromonetny per., Moscow 119017, Russia

ARTICLE INFO

Keywords:
Invisible gold
Pyrite
Sulfur radical ions
High-energy resolution fluorescence-detected x-ray absorption spectroscopy (HERFD-XAS)
Solubility
Chemisorption
Gold deposits

ABSTRACT

The most characteristic feature of hydrothermal deposits of gold is its intimate association with pyrite. Microscopically visible gold occurs in pyrite ore as metal particles of > 0.1 μm in size, together with so called "invisible" gold, undetectable by conventional microscopic methods. The chemical, redox and structural state of this invisible gold and the mechanisms of its incorporation into pyrite remain both inconsistent and controversial since the dawn of economic geology. To clarify these issues, we performed laboratory experiments to simulate interactions of gold-bearing sulfur-rich hydrothermal fluids with arsenic-free pyrite at temperatures from 350 to 450 °C and pressures from 400 to 700 bar, typical of the formation conditions of many types of gold deposits. Gold solubility was measured in these fluids as a function of sulfur speciation and acidity. Gold redox and structural state in pyrite was characterized by high-energy resolution fluorescence-detected x-ray absorption spectroscopy (HERFD-XAS), together with more traditional analytical techniques such as scanning electron microscopy (SEM), x-ray diffraction (XRD), electron probe micro analysis (EPMA), laser ablation inductively coupled plasma mass spectrometry (LA-ICPMS), and inductively coupled plasma atomic emission spectrometry (ICP-AES). Results show that dissolved Au in sulfide-sulfate solutions forms complexes with hydrogen sulfide, and tri- and di-sulfur radical ions whose amounts depend mostly on the fluid pH and total sulfur concentration. Invisible gold in pyrite occurs as Au metal submicron- to nano-sized particles and chemically bound Au(I) in the form of (poly)sulfide clusters composed on S-Au-S linear units, similar to those in aqueous complexes. Our findings contest the common belief that Au(I) substitutes for Fe and/or S in the structure of As-poor pyrite. The partition coefficient of Au(I) between pyrite and the fluid, $D_{py/fl}$, is determined to be 0.15 ± 0.07 at 450 °C in a wide range of Au fluid phase concentrations (10–1000 ppm), but much higher $D_{py/fl}$ values, between 10 and 50, are found at 350 °C. These Au partitioning trends coupled with the new data on Au molecular environment in pyrite suggest a control of Au(I) incorporation in the mineral by a chemisorption step. Extrapolated to Au contents of hydrothermal fluids of the Earth's crust which are typically below 1 ppm, our $D_{py/fl}$ values reproduce fairly well the natural Au tenors in As-poor pyrites (~0.1–1 ppm Au), which are 100–1000 times lower than those typically observed in arsenian pyrites and arsenopyrites (10–1000 ppm Au at As tenors of 0.01–10 wt%). Our results thus indirectly highlight a key role played by arsenic in gold enrichment in As-bearing iron sulfide ore, a role that yet remains to be fully understood and quantified.

1. Introduction

The most characteristic feature of hydrothermal deposits of gold is its intimate association with iron sulfide minerals, pyrite and arsenopyrite, in which Au concentrations may reach 100–1000 ppm, i.e. almost million times the Au average crustal abundance. Gold affinity for

* Corresponding author.
E-mail address: gleb.pokrovski@get.omp.eu (G.S. Pokrovski).

https://doi.org/10.1016/j.oregeorev.2019.04.024
Received 20 January 2019; Received in revised form 19 April 2019; Accepted 30 April 2019
Available online 30 April 2019

these minerals has been recognized since the first half of the 20th century (e.g., Goldschmidt, 1937). Both 'visible' native gold (i.e., optically detectable particles > 0.1–1 μm) in physical association with pyrite, and 'invisible' (i.e., optically undetectable) gold, possibly incorporated into the mineral structure, occur (e.g., Boyle, 1969; Cathelineau et al., 1989; Cook and Chryssoulis, 1990; references therein). Invisible gold, also termed refractory gold, is not only difficult to identify, but also hard to recover from ore (e.g., Yang et al., 1998; Adams, 2005; Marsden and House, 2009). Such refractory gold poses problems both for accurate estimates of the gold distribution and endowment of a deposit and for efficient extraction of the metal from iron sulfide ore. Resolving these issues requires knowledge of the nature, distribution and mechanisms of incorporation of invisible gold in pyrite, which all yet remain enigmatic. The present study was designed in an attempt to better understand the gold-pyrite relationships, using a novel integrated experimental, spectroscopic and modeling approach.

The literature on Au-bearing pyrite over the four last decades is full of discussions about the chemical and redox state of invisible gold. Based on a variety of analytical techniques such as scanning electron microscopy (SEM), high resolution transmission electron microscopy (HRTEM), secondary ion mass spectrometry (SIMS), laser ablation inductively coupled plasma mass spectrometry (LA-ICPMS), electron probe microanalyzer (EPMA), Mössbauer spectroscopy (MBS), proton induced x-ray emission (PIXE), x-ray photoelectron spectrometry (XPS), x-ray absorption spectroscopy (XAS), atom probe microscopy (APM), atomic force microscopy (AFM), tunneling spectroscopy (STS), coupled with analyses of elemental distribution and inter-element correlations, most studies agree that invisible gold occurs in two major chemical states: an elemental form as nanometer-size particles of Au(0) or alloys with some other trace metals (e.g., Bi, Te, Ag), and a chemically bound form (e.g., Marion et al., 1986; Arehart et al., 1993; Scaini et al., 1998; Friedl et al., 1995; Fleet and Mumin, 1997; Genkin et al., 1998; den Besten et al., 1999; Simon et al., 1999; Tauson, 1999; Cabri et al., 2000; Palenik et al., 2004; Reich et al., 2005, 2006, 2010; Mikhlin et al., 2011; Deditius et al., 2011; Fougerouse et al., 2016; Trigub et al., 2017a). However, despite significant recent advances in analytical and microscopic methods listed above, the nature of this latter type of gold and factors controlling its incorporation in pyrite remain both inconsistent and controversial. For example, the redox state of chemically bound gold varies from Au^{3+} to Au^{1-}, and its coordination number from 2 to 6, according to different authors (e.g., see Cabri et al., 2000 for review); such large variations make it difficult to attribute to Au an exact structural position in pyrite and to identify the nature of coordinating atoms (e.g., Au, Fe, S). The situation is further complicated by the presence of other minor and trace elements (Cu, Sb, Ni, Co, Ag, Bi, Se, Te) and, in particular, of arsenic with which gold is systematically correlated in arsenian pyrite (e.g., Reich et al., 2005). These elements, often present in far greater concentrations (> 0.1–1.0 wt%) than Au (typically < 0.01–0.1 wt%), greatly complicate the assessment, using inter-element correlations, of the Au oxidation state and atomic substitutions in pyrite. The use of direct redox-sensitive spectroscopic methods such as X-ray photoelectron, X-ray absorption or Mössbauer spectroscopy is often limited by low concentrations, poor selectivity for Au in the presence of As and other elements, and a lack of adequate standards.

As a result of these limitations, the mechanisms of Au incorporation in hydrothermal pyrite and arsenopyrite and the role of arsenic and other elements played in this process still remain hypothetical. For example, some earlier studies invoked gold transport by the fluid phase in the form of Au-As-S (Sb, Se, Te) aqueous complexes and their co-precipitation with ferrous iron (Boyle, 1969; Boiron et al., 1989). Other studies suggested chemisorption of dissolved Au as Au-S(As) complexes at As-rich, Fe-deficient sites (Mao, 1991; Fleet and Mumin, 1997; Cepedal et al., 2008), electrochemically driven adsorption of negatively charged $Au(HS)_2^-$ complexes on semiconducting As-pyrite and arsenopyrite surfaces (Mironov et al., 1981; Möller and Kersten, 1994; Widler and Seward, 2002), or Au^{3+} and Au^{+} precipitation on sulfide surfaces due to Au reduction (Bancroft and Hyland, 1990; Scaini et al., 1998, Maddox et al., 1998; Mikhlin et al., 2011). However, these hypotheses are mostly based on low-temperature experiments (< 100 °C), some of them involving Au aqueous complexes ($AuCl_4^-$, $Au(CN)_2Br_2^{3-}$), which are unlikely at hydrothermal conditions (e.g., see Pokrovski et al., 2014 for a review of Au speciation in hydrothermal fluids). These limitations complicate the extrapolation of the results of such experiments to the far greater temperatures of Au-bearing pyrite formation in nature (> 150–200 °C). Different isomorphic substitution models of Au in the pyrite structure were also proposed, including coupled substitutions of $As^{3+} + Au^{+}$ for 2 Fe^{2+}, $As^{3+} + Au^{3+}$ for 3 Fe^{2+} (Deditius et al., 2008), $Cu^{+} + Au^{3+}$ for 2 Fe^{2+} (Chouinard et al., 2005), or $Au^{+} + S^{2-}$ for $Fe^{2+} + HS^{-}$ (Tauson, 1999), but analytical methods capable of unambiguously supporting these models are lacking. Note that the geometry of the available structural sites in pyrite composed of $Fe(S_6)$ octahedrons and $S(Fe_3S)$ distorted tetrahedrons (Le Pape et al., 2018) is not favorable for an energetically stable incorporation of both Au^{+} and Au^{3+} ions that have linear and square planar coordination geometries in most inorganic and organometallic compounds (e.g., Cotton and Wilkinson, 1988). Furthermore, common precipitation mechanisms of As and Au due to fluid reduction and/or cooling, or coupled As-Au redox reactions on the pre-existing (arseno)pyrite have also been considered (e.g., Heinrich and Eadington, 1986; Pokrovski et al., 2002), but they remain qualitative owing to the complexity of the fluid composition and evolution in hydrothermal systems and the interplay of multiple factors controlling mineral solubility such as temperature (*T*), pressure (*P*), redox, acidity (pH), and fluid composition (Pokrovski et al., 2014).

It follows from this brief overview that a deeper understanding of the gold-pyrite(-arsenic) relationships in hydrothermal systems awaits experimental studies at pertinent laboratory-controlled conditions, coupled with Au-selective in situ spectroscopic techniques. In the recent years, advances in synchrotron-based high-resolution X-ray absorption/fluorescence spectroscopy (e.g., Proux et al., 2017; Manceau et al., 2018; Le Pape et al., 2018; references therein) have provided an unprecedented gain both in sensitivity (metal detection limits < 1 ppm) and selectivity (ability to isolate the trace metal fluorescence signal in a complex mineral/organic matrix), now enabling to directly "see" invisible gold in iron sulfide minerals. In this study, we designed hydrothermal experiments aimed at investigating the Au-pyrite interactions in model S-bearing fluid-pyrite systems at temperatures (350–450 °C) and pressures (400–700 bar) typical of those of various types of gold deposits, as a function of gold and sulfur speciation in the fluid phase. The Au-bearing pyrites resulting from such experiments were investigated by high-resolution X-ray absorption spectroscopy (HR-XAS) coupled with more "traditional" methods (EPMA, SEM, XRD, LA-ICPMS, ICP-AES) to reveal the state of invisible gold in pyrite and to derive pyrite-fluid partition coefficients for chemically bound Au. The results allow predictions of invisible Au contents in ore, and more reliable identification of the factors leading to Au enrichment in iron sulfide minerals. Although the present work deals with As-free systems, the results also help indirectly assess the role of arsenic, thus providing the foundation for future experimental and analytical studies on far more complex As-bearing systems.

2. Materials and methods

2.1. Experimental strategy and conditions

The primary goal of this exploratory experimental study was to investigate the state of gold incorporated into pyrite under conditions pertinent to natural hydrothermal systems forming gold deposits. Gold incorporation in pyrite is expected to occur via *i)* exchange of an Au-bearing aqueous fluid with already existing sulfide minerals, and/or *ii)* simultaneous precipitation of gold and pyrite (and other metals) from

an aqueous fluid, driven by changes in *T*, *P* or fluid composition. Such fluid-mineral interactions are very difficult to track from the observation of complex natural mineral assemblages; alternatively, they may be simulated experimentally in simplified but well-controlled systems. In this study, we designed two types of experiments to reproduce the two major types of expected Au-pyrite interactions, fluid-mineral exchange and co-precipitation.

Most previous laboratory syntheses of Au-bearing (arseno)pyrite were performed either in dry (salt-flux method) or water-bearing systems at temperatures above 450–500 °C from mixtures of native elements with no control of redox potential, pH, and sulfur speciation, or from pre-existing pyrite and fluid with excess of native sulfur leading to extremely acidic solutions (e.g., Fleet and Mumin, 1997; Tauson, 1999; Trigub et al., 2017a). Such conditions are rather far from those encountered in natural Au-forming hydrothermal systems, which are characterized by moderate temperatures (≤450 °C), and near-neutral pH and redox environments allowing coexistence of sulfate and sulfide in the fluid phase (Pokrovski et al., 2014, 2015). Thus, in contrast to those works, our experiments were conducted in S-bearing gold-saturated fluids at temperatures 350–450 °C and pressures 400–700 bar, and in the presence of sulfide and sulfate over a pH range 4–8. Our experiments allow accurate control on the concentration and speciation of Au and S in the fluid phase, enabling to link, for the first time, both Au status and degree of partitioning in pyrite to the fluid composition and Au aqueous speciation. A scheme summarizing the experimental conditions and major steps is given in Fig. 1.

The run temperatures were chosen to be in the upper range of the common temperature window of most Au-bearing pyrite deposits (150–500 °C) to facilitate mineral-fluid exchange and attainment of equilibrium within the short-time laboratory scale. Aqueous solutions of potassium thiosulfate ($K_2S_2O_3$) with HCl or KOH to adjust the pH were used in both types of experiments. In aqueous solution above 200 °C, thiosulfate breaks down within hours to sulfate (HSO_4^-/SO_4^{2-}) and sulfide (H_2S/HS^-) as the dominant sulfur species with variable amounts of the radical sulfur ions ($S_3^{\cdot-}$ and $S_2^{\cdot-}$) and molecular sulfur (S_n^0), whose fractions depend on pH, temperature and S total amount. Their concentrations can be predicted using the thermodynamic properties derived from in-situ Raman spectroscopy data on similar thiosulfate solutions (Pokrovski and Dubessy, 2015). Importantly, our S-bearing systems enable both f_{O2} and pH buffering via sulfide-sulfate and sulfate-hydrogen sulfate equilibria (Jacquemet et al., 2014), which is essential for interpretation of gold solubility and speciation and can be quantified using thermodynamic modeling (Section 2.8). The choice of elevated S concentrations in this study (1–6 wt% total S), as compared to most natural systems, was dictated by the necessity to solubilize sufficient amount of gold into the fluid to favor fluid-mineral exchange and Au incorporation into pyrite in concentrations sufficient to be analyzable by the methods chosen, and in particular by HR-XAS. Our experimental conditions enable an accurate control on equilibrium and robust extrapolations of the obtained structural and partitioning data to natural systems. Metallic gold was used as the Au source in all experiments. Gold solubility in such S-rich solutions was shown to be controlled by hydrogensulfide (HS^-) and trisulfur ion ($S_3^{\cdot-}$) complexes, depending on pH and S concentration (Pokrovski et al., 2015). Thus, the present experiments not only provide an opportunity to verify these and other alternative Au speciation models in a wide pH range, but also they enable, for the first time, the assessment of the impact of changes in aqueous speciation of sulfur and gold on Au incorporation in pyrite.

2.2. Gold bearing fluid-pyrite exchange experiments

Pyrite-fluid exchange experiments were conducted at 450 °C and 700 bar in batch Ti-based alloy reactors of ~20 mL volume (Fig. 1). Details about the reactor design and handling are given in Pokrovski et al. (2002). The reactor was loaded with a weighed amount of aqueous ~0.5 mol/kg (m) $K_2S_2O_3$(-HCl-NaOH) solution. A weighed piece of gold foil (Heraeus, 99.99% purity) was attached to a titanium container suspended in the upper part of the reactor. A weighed amount of

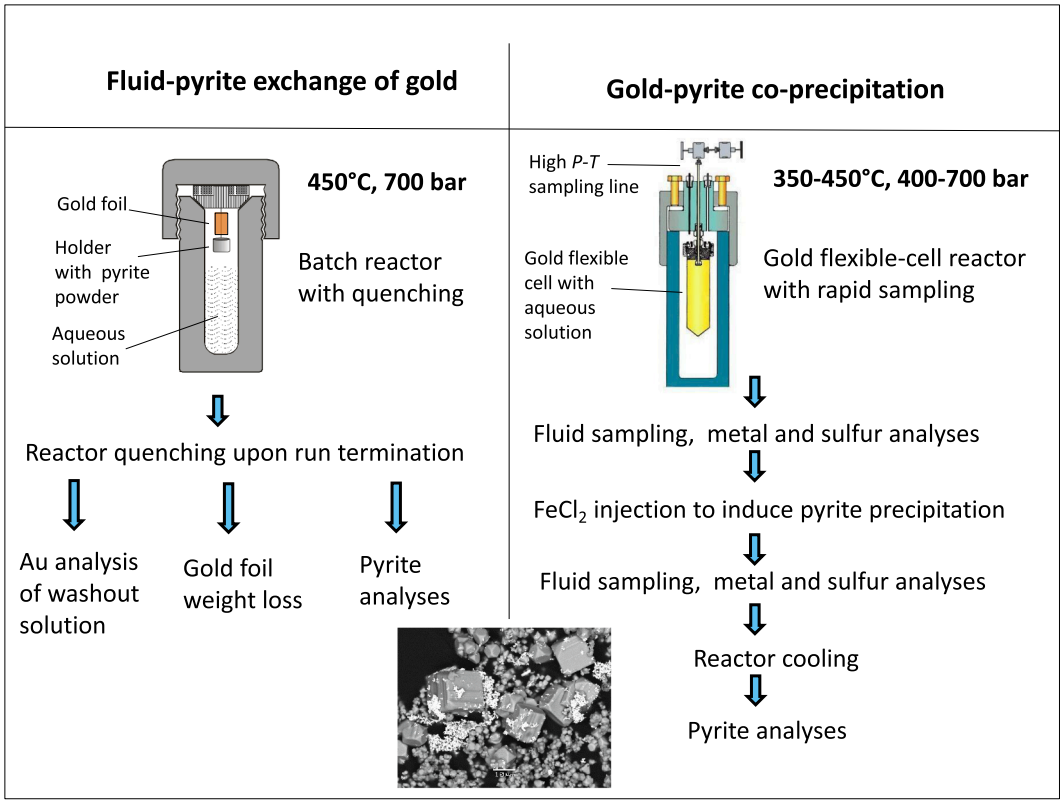

Fig. 1. Schematic illustration of the experimental design and procedures used in this study.

Table 1
Batch reactor experiments: initial system compositions and gold dissolved concentrations determined from gold weight-loss and analyses of quenched fluid from runs conducted in this study at 450 °C and 700 bar.

Run number	Mass of aqueous solution loaded, g	Solids loaded	Mass of Py/Po loaded, g	Initial system composition, mol/kg fluid			Δm_{Au}, mg, weight loss	Au in fluid, ppm, weight loss	Au in quenched fluid, ppm, chemical analysis	Au in solid[c], ppm
				$K_2S_2O_3$	HCl	KOH				
Py1	13.639	Py, Au	1.120	0.50	0.65	–	0.7	47	< 150	ND
Py2	13.460	Py, Au	1.121	0.50	0.20	–	7.3	545	440	1260
Py3	16.843	Py, Au	0.659	0.50	0.20	–	< 0.5	< 30	237	ND
Py4	14.264	Py, Au	1.023	0.50	–	–	22.3	1631	1664	ND
Py5	15.246	Py, Au	0.730	0.50	–	0.31	39.0	2559	2832	ND
Py6[a]	8.786	Py	0.935	0.50	0.20	–	< 0.5	< 60	2	ND
Py7[b]	15.266	Py, Au	1.004	–	–	–	0.5	41	135	ND
Po1	15.324	Po, Au	0.308	0.50	0.20	–	10.0	652	426	6980
Po2	12.984	Po, Au	0.309	0.49	0	0.31	24.6	1608	946	13,800
Error	± 0.010 g		± 0.005 g				± 0.5 mg	± 50 ppm	± 15%	± 20%

[a] Au-free blank run for evaluating Au contamination from the autoclave and washing solutions.
[b] S-poor Au-bearing blank run in water for evaluating detection limits for Au concentration determinations.
[c] Derived from the difference of Au concentrations from weight loss and quenched fluid analyses and using the masses of the loaded solution and solid phase. ND here means not detected; it is applicable to cases where this difference is negative.

iron(II) disulfide (FeS_2, pyrite, powder, 325 mesh, 99.8% trace metals basis, < 10 ppm As, Sigma-Aldrich) or iron(II) monosulfide (FeS, powder, 100 mesh, 99.9% trace metals basis, < 0.1 ppm As, Sigma-Aldrich) was placed into the container, avoiding direct contact with the gold foil. The runs starting with FeS_2 and FeS are named 'Py' (for pyrite) and 'Po' (for pyrrhotite), respectively (Table 1). Before experiments, the solids were characterized by XRD and SEM and, after total digestion in aqua-regia, by ICP-AES (see below); they were found to be free of gold (< 0.01 ppm) and contain only minor (< 0.1 wt%) impurities of $BaSO_4$ (in FeS_2), and of FeS_2 and native Fe and S (in FeS). The reactors were placed in a temperature-controlled oven (± 1°C); the pressure at the run temperature was estimated from the degree of filling of the reactor (which is equivalent of the fluid density at experimental *P-T*), and using the *P-T-X*-density properties of the well-known NaCl-H_2O system (Driesner and Heinrich, 2007) and assuming that the density of a $K_2S_2O_3$(-HCl-KOH)-bearing supercritical fluid is similar to that of an NaCl fluid of the same mass concentration (wt%); this approximation induces an error of less than ± 100 bar at 450 °C and 700 bar (e.g., Pokrovski et al., 2009a).

The run duration was 24 days (except 19 days for Py3 run), which was considered long enough to attain the solid-fluid chemical equilibrium as shown by numerous previous experiments on Au solubility in S-rich systems over a wide *T* range (250–450 °C, Pokrovski et al., 2009a, 2015) as well as by studies of Fe/Ni sulfide recrystallization in the presence of aqueous fluids at temperatures as low as 120 °C (e.g., Xia et al., 2009) that demonstrated attainment of equilibrium within a period of a few hours to a few days. At the end of the experiment, the reactor was placed in water for cooling, resulting in a fast separation of the container with the pyrite phase from the fluid that condenses into liquid in the lower part of the reactor thus avoiding fluid-solid back reactions, then cooled for 20 min, unloaded, and washed 3 times with hot aqua regia to remove all gold that was dissolved in the fluid at the run temperature but (partly) precipitated on reactor walls upon cooling. The resulting washout solution was treated and analyzed for Au (Section 2.4). The solid phase was rinsed with water to remove traces of salt, dried at 50 °C, and analyzed as described below (Sections 2.5 and 2.6). The gold foil was also rinsed with water, dried, and weighed to determine weight loss due to gold dissolution in the fluid and incorporation in pyrite, thus providing an additional control on Au total dissolved concentrations.

2.3. Gold-pyrite co-precipitation experiments

Gold-pyrite co-precipitation was simulated at 350 °C/400 bar (runs Copy1 and 2) and at 450 °C/700 bar (run Copy3, Table 2) using a hydrothermal reactor (Fig. 1) equipped with an ultra-fast sampling device and a flexible inner gold cell (150–180 cm^3), adapted to multi-component S-rich systems similar to those of the present study (Pokrovski et al., 2008; Kokh et al., 2017). The reactor is placed in a rocking furnace and the temperature (± 1°C) and pressure (± 5 bar) are controlled independently during the run. The reactor is equipped with a sampling tube, two high-pressure titanium valves and a titanium vial tightly assembled to the second valve; this design allows for almost instantaneous (within < 1 s) sampling of a portion of the fluid phase pushed by the internal pressure from the reactor, thus avoiding any solute precipitation or degassing, which would have inevitably occurred in S-rich systems using traditional sampling procedures. The cell was loaded with an aqueous thiosulfate solution and the reactor was brought to the desired *P-T*; the fluid was periodically sampled to monitor attainment of gold solubility equilibrium, and processed and analyzed as described below (Section 2.4). The composition of the fluid may be modified in situ at high *P-T* during the run via injection, using a calibrated capstan pump, of a given amount of another solution (e.g., HCl in CoPy3 experiment) inducing controlled changes in pH and Au solubility. Furthermore, in the final step of the three CoPy experiments, an $FeCl_2$ solution was injected into the cell, inducing pyrite precipitation followed by re-equilibration between the precipitated pyrite and the fluid of modified composition. At the run termination, the reactor was cooled down within a few hours and the pyrite precipitate was recovered. Compared to the batch reactor technique (Section 2.2), the flexible-cell reactor enables far more accurate, time- and composition-resolved measurement of gold solubility and sulfur speciation in the fluid at high *P-T*, but does not allow fast recovery of the solid phase that might potentially be subject to some modifications (e.g., Au precipitation or re-dissolution) during the inevitably slow cooling of the 80-kg reactor.

2.4. Chemical analyses of experimental solutions

Chemical treatment and analyses of gold, other metals and sulfur in the experimental solutions were performed using protocols developed in Kokh et al. (2016, 2017). Briefly, Au concentrations in aqua-regia washout solutions from experiments in batch reactors were analyzed by ICP-MS and/or ICP-AES. The sample preparation recipe consists of gentle evaporation of the aqueous sample on hot plate (at 60–80 °C) in a clean Teflon vial (Savilex©) until a wet salt residue is obtained; then reacting the residue with 2 g of hot aqua regia in the closed vial (at 120 °C for ~2 h), followed by gentle evaporation of the solution to

Table 2
Flexible-cell reactor experiments: fluid composition and gold and other element dissolved concentrations measured in sampled fluids of $K_2S_2O_3$(-HCl-KOH-$FeCl_2$) composition at the indicated *P-T*-time conditions. Also reported are the initial aqueous solution compositions and concentrations of the compounds injected into the experimental fluid. Concentrations of major solute components are in mole per 1 kg of fluid (m); those of Au in ppm.

Run name, sample number	Days from start	S_{tot}	sulfide	sulfate	K	Cl	Fe	Au, ppm
CoPy1	350 °C, 370 bar; 0.49 m $K_2S_2O_3$ + 0.14 m HCl							
1	1	1.00	0.31	0.40	1.00	0.13	1×10^{-5}	653
2	3	1.07	0.31	0.42	1.02	0.13	2×10^{-5}	709
3	7	0.95	0.30	0.41	0.92	0.13	2×10^{-5}	625
4	10	0.97	0.30	0.39	0.97	0.13	1×10^{-5}	556
Injection of KCl (0.11 m)-$BaCl_2$(0.090 m)-$FeCl_2$ (0.18 m)								
5	14	0.26	0.0043	0.21	0.86	0.74	0.027	6
6	17	0.25	0.0050	0.20	0.88	0.74	0.023	16
7	24	0.24	< 0.003	0.19	0.86	0.75	0.014	37
CoPy2	350 °C, 400 bar; 0.19 m $K_2S_2O_3$ + 0.091 m KOH							
1	1	0.37	0.16	0.14	0.58	< 0.02	4×10^{-5}	474
2	3	0.33	0.11	0.13	ND	< 0.001	5×10^{-5}	403
Injection of $FeCl_2$ (0.056 m)								
3	14	0.12	< 0.001	0.12	0.49	0.20	0.0022	51
4	17	0.11	< 0.001	0.084	0.44	0.19	0.0014	51
CoPy3	450 °C, 700 bar; 0.50 m $K_2S_2O_3$ + 0.30 m KOH							
4	16	0.71	0.40	0.32	0.79	ND	ND	1552
5	20	0.69	0.35	0.24	0.78	ND	ND	1358
6	23	0.75	ND	ND	0.93	ND	ND	1365
7	27	0.59	0.37	0.28	0.60	ND	ND	1299
Injection of HCl (0.172 m)								
8	29	0.62	0.20	0.35	0.74	0.20	ND	561
9	32	0.57	0.19	0.31	0.68	0.18	ND	638
10	35	0.54	0.25	0.32	0.61	0.22	ND	563
Injection of $FeCl_2$ (0.051 m)								
11	37	0.43	0.13	0.33	0.68	0.27	ND	148
12	41	0.47	0.11	0.28	0.76	0.29	ND	49
13	44	0.48	0.084	0.30	0.75	0.28	ND	75
Error		± 10%	± 10%	± 10%	± 10%	± 10%	± 50%	± 10%

ND = not determined.

0.2–0.3 g (at 60–70 °C), and finally dilution of the rest by ultra-pure doubly-distilled 0.5 wt% HCl – 1.5 wt% HNO_3 in water. Gold, K and Fe in the fluids from experiments in the flexible-cell reactor were treated and analyzed using the same protocol for fluids sampled into an NH_3 (28 wt% NH_3 in water) solution (Kokh et al., 2016). The overall analytical uncertainties (which include sample treatment and ICP-MS or ICP-AES analysis) on the final concentration do not exceed 10% of the value.

Chlorine and sulfur were also analyzed in fluids sampled from the flexible-cell reactor. Total chloride was quantified (as the Cl^- ion) by high-performance liquid chromatography (HPLC). Total dissolved sulfur (S_{tot}) was analyzed by ICP-AES and/or HPLC (as the SO_4^{2-} ion) after complete oxidation to sulfate in NH_3-H_2O_2 solutions. Both methods for S showed an agreement within 10% of the total concentration value. Total reduced sulfur (S_{red}, dominantly hydrogen sulfide, and eventually sulfite and polysulfide) was quantified by iodometric titration. Hydrogen sulfide (H_2S/HS^-) was separated from the other sulfur species by precipitation as cadmium sulfide (CdS) and centrifugation, followed by iodometric titration of CdS in acid solution (10 wt% HCl). Because the concentrations of reducted sulfur and sulfide were identical within error, only sulfide is reported in Table 2. Sulfate was analyzed gravimetrically from the fluid sampled directly in a 1 m Ba acetate solution resulting in precipitation of $BaSO_4$, which was subsequently washed, centrifuged, and dried before weighing. Uncertainties of the Cl and S analyses are < 10% of the value. The concentrations of Au and other solutes in batch and flexible-cell reactor experiments are reported in Tables 1 and 2, respectively.

2.5. Conventional analyses of experimental pyrites

The solids recovered from both types of experiment were analyzed for phase composition and major element contents by XRD, SEM and EPMA (Table 3). The analyses showed pyrite as the major phase with variable amounts of visible gold particles (0.1–10 μm) in almost all experiments, plus minor pyrrhotite (< 5%) in the two batch-reactor runs started with FeS (Po1 and Po2, Table 1, Fig. 2). Total gold was quantified by dissolution of a weighed amount of the bulk pyrite solid in hot aqua-regia, followed by the same treatment as that for the aqueous solutions (Section 2.4) and ICP-AES analysis. Visible gold contents were also independently estimated on polished sections by SEM-EDS mapping of a given surface area (typically ~1 mm^2). The surface of gold particles, being much brighter in back scattered electron (BSE) mode than pyrite (e.g., Fig. 2), was measured and compared to the surface of all pyrite grains using the ImageJ software. The visible Au concentration (in ppm) was then estimated as:

$$C_{Au(0)}(ppm) = (S_{Au(0)} \times \rho_{Au} \times 10^6)/(S_{Pyrite} \times \rho_{Pyrite}) \quad (1)$$

where $S_{Au(0)}$ and S_{Pyrite} are the surfaces of gold and pyrite grains respectively, and ρ_{Au} and ρ_{Pyrite} are the densities of pure metallic gold (19.3 g/cm^3) and pyrite (5.0 g/cm^3), respectively. Although these analyses are subject to large uncertainties due to the potentially limited representativeness of the examined polished surfaces and SEM resolution, they nevertheless provide a useful estimate of visible gold content for Au-rich samples (> 0.1 wt% total Au).

An attempt was also made to analyze invisible Au in large pyrite crystals (> 10 μm), by carefully avoiding visible Au particles, using EPMA (Cameca SX Five microprobe, electron beam spot ~1 μm, accelerating voltage 25 kV, current 100 nA, counting time 240 s). All analyses for the fluid-pyrite exchange runs (Py and Po series) were, however, only a factor of ~2 above the EPMA detection limit of ~120 ppm Au, in agreement with low invisible gold concentrations found by X-ray absorption spectroscopy in these samples, whereas the co-precipitation runs (CoPy series)

Table 3
Total gold, visible and invisible native gold, and invisible chemically bound gold concentrations in pyrite from hydrothermal batch-reactor and flexible-cell reactor experiments of this study obtained using different analytical methods.

Run	Acid digestion and ICP-AES; Au total, ppm	SEM; Au visible			EPMA[a]; Au invisible, ppm (Nb pts)	LA-ICPMS[b]; Au invisible, ppm (Nb pts)	X-ray Fluorescence[c]; Au invisible		% Au(I) LCF XANES of Au invisible	Au(I) chemically bound in pyrite, ppm[d]
		S_{Au}, μm^2	S_{Py}, μm^2	Au^0, ppm			$\Delta\mu_{fl} \times 10^4$	Au invisible, ppm		
Py1	100	2.7	68,017	150	180 (30)	ND	0.531	52	95	50
Py2	117	3.2	57,915	210	180 (21)	81 (9)	0.598	59	> 97	58
Py3	ND	ND	ND	ND	ND	ND	0.552	48	88	42
Py4	605	3.2	60,696	201	180 (29)	ND	4.81	471	30	141
Py5	486	51	307,653	639	190 (27)	180 (8)	2.08	204	> 97	204
Po1	5591	470	82,194	23,941	ND	320 (9)	13.73	1190	4.5	54
Po2	20,418	410	89,092	19,286	ND	ND	16.25	1593	7.3	116
CoPy1	ND	ND	ND	ND	4000 (20)	ND	36.57	3586	46	1664
CoPy2	ND	ND	ND	ND	5000 (45)	ND	129.7	12,716	5	636
CoPy3	ND	ND	ND	ND	ND	6047 (5)	132.2	12,957	< 3	< 390
Error	± 5%			± 50%	± 50%	± 50%	± 15%	± 20%	± 3%	± 25%

ND = not determined.
[a] EPMA detection limit is 120 ppm Au.
[b] LA-ICPMS typical detection limit is 0.1 ppm Au
[c] XRF detection limit is 1 ppm Au.
[d] Obtained as the product of Au(I) mole fraction and the total Au concentration from fluorescence spectra from Eq. (2).

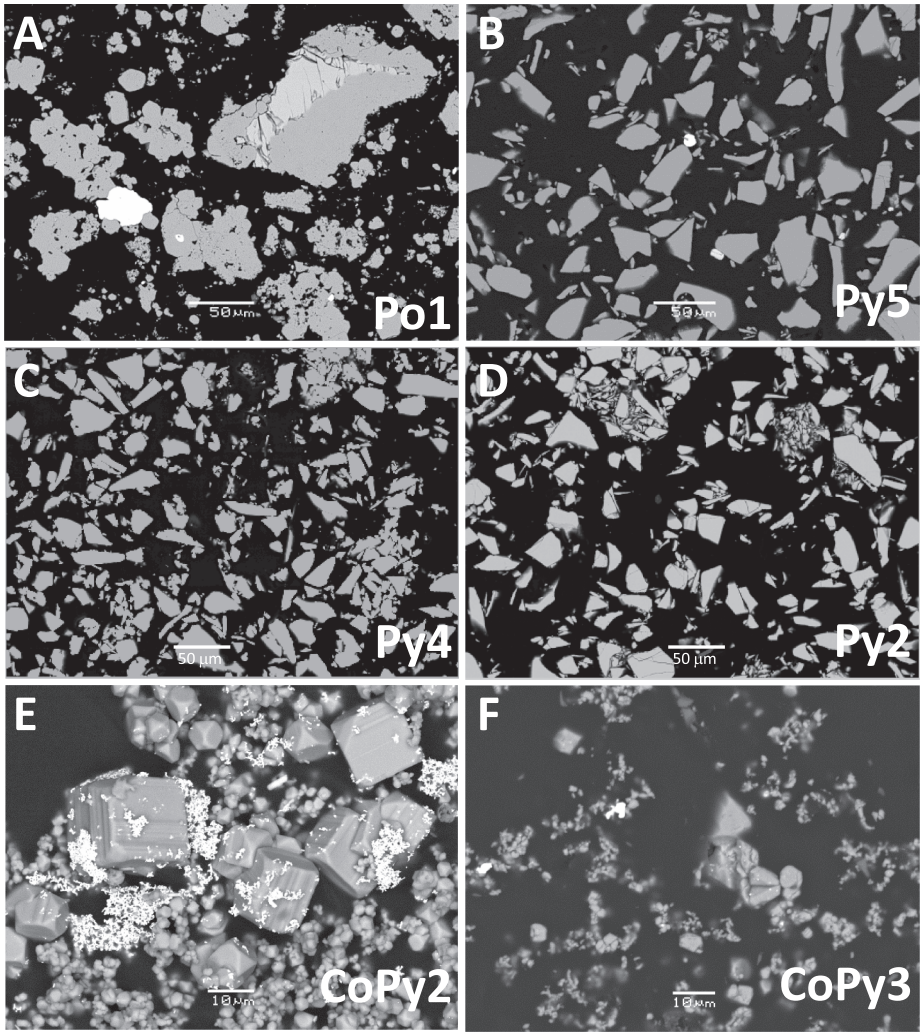

Fig. 2. Scanning Electron Microscopy (SEM) microphotographs in back scattered electron (BSE) mode of representative pyrite samples from hydrothermal experiments in the presence of dissolved gold (see Tables 1 and 2) for sample identity and composition). Visible metallic gold is manifested by microscopic bright particles associated with grey grains of pyrite of variable size and morphology. (A) Pyrite (grey) with rests of initial pyrrhotite (light grey) and visible native gold grains (white) from acidic solution (run Po1). (B) Pyrite and native gold from an alkaline solution (Py5). (C) and (D) Pyrites with no visible native gold, from neutral (Py4) and acidic (Py2) solutions, respectively. (E) and (F) Pyrite powder and polished section, respectively, from co-precipitation experiments (CoPy2 and CoPy3) with metallic gold particles of variable size, from < 0.1 to ~ 2 μm. (For interpretation of the references to color in this figure legend, the reader is referred to the web version of this article.)

yielded much higher Au contents (1000 s ppm), which match the XAS-determined concentrations within a factor of 2 (Section 2.6).

Selected samples were also analyzed for Au by LA-ICPMS using a Finnigan MAT Element equipped with a femtosecond UV laser (laser spot diameter ~20 μm yielding an ablation crater of 25–30 μm, energy 0.003 mJ, fluency 0.94 J/cm^2, power 12%, frequency 5 Hz, background time 45 s, ablation time 60 s). Transient ablation signals were converted to concentration using the SILLS software (Guillong et al., 2008), and an external Au-bearing FeS standard (LaFlamme Po726 standard reference material, 46 ± 2 ppm Au, Sylvester et al., 2005) and Fe content in pyrite as the internal standard. Although the LA-ICPMS technique offers much higher sensitivity compared to EPMA, with typical detection limits of 0.1 ppm Au for our samples, the major challenge of such analyses is the small pyrite grain size being typically < 10–40 μm with rare exceptions (Fig. 2), which is smaller than or comparable to the ablation spot size. In addition, the LA-ICPMS analysis is much more penetrative than EPMA, with ablation depth superior to the beam spot diameter (> 20 μm). As a result, these analyses of individual pyrite grains (by avoiding "visible" > 1 μm gold particles, where possible), allow only a rough estimate of total invisible gold content, and provide information about Au distribution across the grain depth. This analysis cannot exclude the presence of gold nuggets inside or underneath a pyrite grain. An attempt to reduce the laser spot to 5 μm allowed elimination of some of the largest spikes, but yielded too unstable and weak ablation signals to obtain accurate analytical results for our particular samples. Recent developments of LA-ICPMS time-of-flight setups (e.g., Gundlach-Graham et al., 2018) would enable, in near future, high-resolution quantitative elemental imaging of gold and other trace metals in analytically challenging pyrite samples like those of the present study.

2.6. High-resolution X-ray absorption spectroscopy (HR-XAS) analyses of experimental pyrites

HR-XAS analyses at the Au L_3 edge (~11.920 keV) of experimental pyrite samples were performed at FAME (BM30b) beamline of the European Synchrotron Radiation Facility, Grenoble, France (Proux et al., 2005), using a recently developed 5-crystal spectrometer operating in high-energy resolution fluorescence detected (HERFD) mode (Llorens et al., 2012). The two main advantages of using HERFD compared to traditional XAS spectroscopy are *i)* a significant gain in spectral resolution compared to nominal resolution defined by the core hole width of the absorption edge, allowing the detection of different features in X-ray absorption near-edge structure (XANES) spectral region, which are indicative of Au redox state and coordination geometry, and *ii)* the ability to efficiently filter out all unwanted contributions from elastic scattering and fluorescence from other elements (e.g., As whose absorption edge is within 50 eV of that of Au) in the sample and thus significantly improve both the limit of detection for Au and signal-to-noise ratio of XAS spectra. In addition, L_3-edge XANES spectra at nominal resolution of most Au(I) compounds and complexes with common ligands (S, Cl, P) are quite similar and rather featureless (Fig. 3; Pokrovski et al., 2009a,b, 2015), making it difficult to unambiguously distinguish between the different Au coordination environments and the identity of neighboring atoms.

The beamline X-ray optics incorporated a Si(2 2 0) double crystal monochromator with sagittal focusing providing a beam spot (full width at half maximum, FWHM) of 200 × 300 μm^2 at the sample, Rh-coated mirrors for harmonic rejection, and a crystal analyzer spectrometer (Llorens et al., 2012) with five Si(6 6 0) crystals placed in a Roland circle geometry (Bragg angle = 85.71°). This device allows a resolution of 1.3 ± 0.1 eV at the Lα Au fluorescence line measured as FWHM of the elastic peak, providing a gain in resolution by a factor of ~5 compared to nominal spectral resolution (natural core-hole width is 5.4 eV at the Au L_3-edge). High-resolution fluorescence XANES (hereafter HR-XANES) spectra were recorded using a Vortex EX-90 mono-element detector. In addition, nominal-resolution transmission spectra were acquired at the same time as HERFD spectra for all samples and reference compounds. The pyrite samples from hydrothermal experiments were homogenized by mild grinding, which was necessary for obtaining XAS signals devoid of harmonics, diffraction peaks, spectral distortions, and self-absorption artifacts which are all common for inhomogeneous samples (e.g., Curis et al., 2005; references therein). The produced powders were pressed in 5-mm diameter pellets, affixed with silicon grease to a copper holder and placed in a liquid He cryostat (~10 K) to reduce X-ray beam-induced damage common for redox-sensitive elements like Au (Pokrovski et al., 2009b). A helium-filled bag was placed to fill the space between the crystal analyzers, cryostat window where the pyrite sample is placed, and detector, to reduce the absorption of the Au fluorescence signal by air. Different reference Au-bearing compounds (Au, Au_2S, $Na_3Au(S_2O_3)_2{\cdot}1\text{-}2H_2O$, AuAgS, Au-thiomalate, $KAuCl_4{\cdot}1\text{-}2H_2O$, $AuTe_2$, Au-doped CuS, $AuSb_2$, and AuClP$(Phen)_3$ and $AuCl(P(Phen)_3)_2$ where Phen is the phenol cycle C_6H_5OH) were diluted by mixing with boron nitride powder to obtain an Au concentration of 1–2 wt%, comfortable for fluorescence measurements but low enough to avoid self-absorption effects that lead to damping of XANES amplitudes. The prepared powders were pressed in pellets and recorded similarly to the pyrite samples, both in transmission (nominal resolution) and fluorescence (high resolution) modes.

Since our pyrites contain both visible and invisible gold (Fig. 2), care was taken to avoid gold particles larger than ~1 μm and to assure relative homogeneity of Au concentrations over the whole beam size during the acquisition, which is essential for obtaining accurate and reproducible XAS spectra. The acquisition spots were thus carefully chosen by scanning the pellets in two directions (e.g., Fig. A1). The X-ray beam was positioned sufficiently far from large fluorescence peaks arising from gold particles to allow us to probe essentially invisible and relatively homogeneously distributed gold in the sample. For most pyrite samples of low Au concentration (< 100 ppm) multiple scans (5–20) were recorded and, if found similar, merged together to increase the signal-to-noise ratio. The concentration of invisible gold in pyrite in the acquisition spots may directly be determined from the edge height of the fluorescence spectrum using a standard of known Au concentration with similar matrix major elements (Fe, S), measured at identical acquisition conditions. The standard used in this study is a mixture of natural Au-bearing pyrite and arsenopyrite from the Villeranges deposit, France (sample MCB-7358) in which gold is present exclusively in a chemically bound state as demonstrated by Mössbauer spectroscopy (Boiron et al., 1989). Total concentrations of Fe, S, As and Au in the standard were determined by ICP-AES after complete aqua-regia digestion of the solid. The obtained solid composition corresponds to the formula $FeAs_{0.28}S_{1.72}$ with 450 ± 50 ppm Au. The solid was ground, pressed in a pellet, and measured by XAS similarly to the experimental pyrite samples (detailed account of Au XAS spectra of this and other natural and synthetic arsenian pyrites and arsenopyrites will be given elsewhere). Gold concentrations in our pyrite samples were thus determined using proportionality between absorption edge height in fluorescence mode ($\Delta\mu_{fl}$) and Au concentration for a pyrite sample (Py) and the standard (St):

$$C_{Au}(Py) = \Delta\mu_{fl}(Py) \times C_{Au}(St)/\Delta\mu_{fl}(St) \quad (2)$$

HR-XANES spectra were normalized to the absorption edge height with the Athena software (Ravel and Newville, 2005) to compare with spectra of reference compounds and perform linear combination fits (LCF) to quantify the contributions from different Au structural environments and to directly distinguish between native and chemically bound gold. Furthermore, the experimental XANES spectra were compared with quantum-chemically simulated ones for different Au cluster geometries and substitution models in pyrite. Due to relatively low Au concentrations, the insufficient signal-to-noise ratio of most pyrite samples did not allow acquisition of extended x-ray absorption fine structure (EXAFS) spectra good enough to extract accurate structural

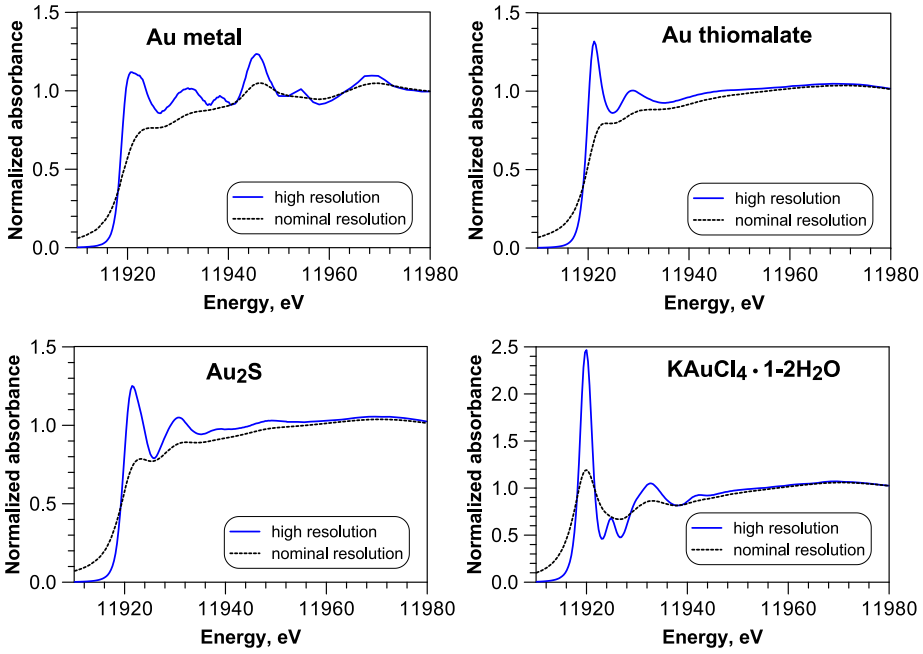

Fig. 3. Comparison of Au L_3-edge XANES spectra of representative gold-bearing compounds recorded in nominal resolution (dashed line) versus high-resolution HERFD (solid blue line) mode. Note that the nominal-resolution spectra for most Au(0) and Au(I) compounds are rather featureless with weak white line intensities and poorly resolved after-edge resonances. In contrast, spectacular improvement in spectral resolution is apparent in HERFD mode, with each spectral feature neatly emphasized, which allows unambiguous comparisons among samples and quantitative analyses of the different Au states in samples with multiple Au chemical environment (e.g., using LCF). (For interpretation of the references to color in this figure legend, the reader is referred to the web version of this article.)

information. Most EXAFS spectra had low signal-to-noise ratios and short exploitable energy ranges ($3 < k < 8$ Å^{-1}, where k is photoelectron wavenumber), which resulted in large errors on Au nearest coordination numbers ($2 < N < 6$ atoms) and interatomic distances ($2.2 < R < 2.4$ Å). As a result, in this study we rely on the analyses of the HR-XANES experimental and quantum-chemistry simulated spectra.

2.7. Quantum-chemistry ab-initio modeling of XANES spectra using FDMNES

Direct and unambiguous interpretation of XANES spectra, particularly in high-resolution mode, requires reference compounds with Au redox and structural environments closely matching those of the samples. Since no such stable compounds with known structures exist in the Au-Fe-S(-As) system, a theoretical simulation of XANES spectra for expected Au geometries and structures in pyrite is the only alternative. Such simulations become now possible due to significant progress in quantum-chemical modelling of full electron potential in the near-edge absorption region, coupled with increasing computer power enabling the use of Fine Difference (FD) methods for solving the Schrödinger equation on the node points of a three-dimensional grid (Amestoy et al., 2006; Guda et al., 2015). We used the FDMNES code (Joly, 2001; Bunau and Joly, 2009) to calculate theoretical Au L_3-edge XANES spectra of different possible Au local structures and geometries in pyrite (e.g., Au substitution in the Fe or S structural sites, different Au-S_n clusters similar to those in aqueous solution adsorbed on pyrite surface) and to compare them with the experimental spectra. All calculations were performed in FD mode (note that in case of low symmetry, the muffin-tin approximation is not sufficient in the near-edge energy range; Joly, 2001; Testemale et al., 2004), and accounting for relativistic effects and spin-orbit interactions intrinsic to heavy atoms such as gold (program's keywords 'Relativism' and 'Spinorbit'; Joly, 2018). The obtained raw calculations represent the evolution of the photo-absorption cross-section of Au as a function of X-ray photon energy and correspond to the transition amplitude between the initial and final states with an energy resolution of the FD method (< 0.1 eV). These spectra, which display almost all possible electronic transitions, are further convoluted with a Lorentzian function (keyword 'Arc') with a width of 1.3 eV (keyword 'Gamma_hole'), which corresponds to the energy resolution of our HERFD setting (Section 2.6).

2.8. Thermodynamic calculations in experimental fluid-mineral systems

Gold and sulfur speciation and solubility in the fluid phase of the experimental systems were modelled using available robust thermodynamic data, and the results were compared with the measured Au solubility. Calculations were performed using the HCh software package and associated Unitherm database, allowing chemical equilibrium simulations in multicomponent fluid-mineral systems based on the minimization of the Gibbs energy of the system (Shvarov, 2008; 2015), and accounting for non-ideality of the fluid using the extended Debye-Hückel equation (Helgeson et al., 1981). The selection of thermodynamic data sources was discussed in detail elsewhere (Pokrovski et al., 2015; Kokh et al., 2017), and will only briefly be summarized here.

The thermodynamic properties of the minerals, major fluid components, and most sulfur aqueous species were taken from the updated SUPCRT (Johnson et al., 1992), JANAF (Chase, 1998), and Robie and Hemingway (1995) databases, complemented by recent data for ionic sulfur forms including S_3^- (Pokrovski and Dubessy, 2015; references therein) using the revised and extended HKF (Helgeson-Kirkham-Flowers) equation of state (Oelkers et al., 2009; Sverjensky et al., 2014; references therein). The thermodynamic properties of the molecular sulfur aqueous forms, H_2S, SO_2 and H_2 and O_2, were adopted according to a recent model for aqueous non-electrolytes (Akinfiev and Diamond, 2003), which allows a more accurate description over the *P-T* range relevant to our study (350–450 °C; < 1 kbar) than the SUPCRT database, which used a more limited experimental dataset in derivation of the HKF model coefficients for these species. Noteworthy, the thermodynamic data from Akinfiev and Diamond (2003) were also used in derivation of the thermodynamic properties of Au species (see below), and thus were chosen here to maintain thermodynamic consistency.

The thermodynamic properties of the Au^+ cation, and its traditional hydrogen sulfide (AuHS, $Au(HS)_2^-$) and hydroxide (AuOH) species were taken from a recent compilation of Pokrovski et al. (2014), consistent with most recent experimental data. The Gibbs energy value of the dichloride species ($AuCl_2^-$) for which there is a more substantial disagreement among the major data sources, was taken as an average between those reported in Pokrovski et al. (2014) and Stefánsson and Seward (2003). Species such as AuCl and $Au(OH)_2^-$, tentatively suggested in some previous compilations, were ignored in the present modeling both because their existence in hydrothermal solutions is not

explicitly proven by direct experimental data and their parameters are based on estimations at ambient conditions and thus are subject to large errors at elevated temperatures. Among the traditional species, only $Au(HS)_2^-$ was found to significantly contribute to the measured Au solubility in our S-rich systems at near neutral pH. The recently discovered gold complex with the trisulfur ion, $Au(HS)S_3^-$ (Pokrovski et al., 2015), accounting for Au solubility in acidic-to-neutral solutions, was also included in the model. In addition, a tentative Au complex with the disulfur radical ion, $S_2^{\cdot-}$, which has been detected by in-situ Raman spectroscopy in similar thiosulfate aqueous solutions (Pokrovski and Dubessy, 2015), was also tested to account for the measured solubility (Section 4.1). It should be emphasized that our choice of thermodynamic data sources for major sulfur forms and its complexes with gold is self-consistent, which is a key condition for accurate interpretation of Au speciation and solubility in S-rich systems at elevated temperatures, similar to those of the present study (e.g., Pokrovski et al., 2015).

3. Results

3.1. Gold concentration in the fluid phase

3.1.1. Batch-reactor experiments

Gold concentrations measured in quenched solutions from batch-reactor experiments at 450 °C and 700 bar are reported in Table 1. The dissolved Au concentrations vary from ~100 ppm (in acidic solutions) to almost 3000 ppm (in alkaline solutions). A reasonable quantification limit for aqueous Au in our experimental systems is about 100–150 ppm, which is due to intrinsic uncertainties of the batch-reactor technique such as incomplete recovery of Au precipitated on the reactor walls after the quench, possible recrystallization of Au in the reactor during the run due to minor temperature gradients, mechanical detachment of gold metal particles from the foil suspended in the upper part of the reactor, and uncontrolled gold dissolution during the reactor heating or cooling. These artifacts may result either in overestimation or underestimation of the true gold solubility (see Section 4.1). Total gold dissolved concentrations can independently be estimated from weight loss of the gold foil after the experiment (with a reasonable detection limit of ~50 ppm Au and an uncertainty of ± 50 ppm Au corresponding to weight loss of < 0.5 mg). This estimation takes into account Au incorporation in pyrite, but is obviously subject to the same artifacts. It can be seen in Table 1 that for the runs with low Au solubility in the fluid producing Au-poor pyrites (Py1, 3 and 6) the gold weight-loss derived concentrations are similar within errors to those derived from quench-solution analysis. For runs in the presence of initial pyrite and with higher Au aqueous concentrations and less acidic pH (> 400 ppm Au, Py2, 4 and 5), the weight-loss derived concentrations are also in agreement with those from the quenched solution, demonstrating almost complete recovery of gold and a negligibly small (within the associated errors) fraction of the Au incorporated in pyrite. By contrast, runs starting with FeS (Po1, 2) yielded significantly higher weight-loss Au concentrations compared to those derived from quenched solution, demonstrating that a more important fraction of Au was precipitated on and/or incorporated into the solid phase during FeS transformation into pyrite, as also confirmed by direct analyses of the solid phase (Section 3.2).

3.1.2. Flexible-cell reactor experiments

Gold and other solute (S, Cl, K, Fe) concentrations, measured in sampled portions of fluid as a function of time in co-precipitation experiments conducted at 350 and 450 °C using the flexible-cell reactor (Copy1, 2 and 3), are reported in Table 2. It should be emphasized that these direct measurements are not subjected to the artifacts common for the batch-reactor method enumerated above and thus may be considered to represent the true gold solubility values. The uncertainties of Au solubility are < 10% of the total value; they stem mostly from the S-rich solutions treatment and analysis by independent methods (ICP-MS, ICP-AES). It can be seen that Au dissolved concentrations before pyrite precipitation were constant within errors for run durations from 1 to 10 days, demonstrating attainment of saturation with metallic gold. After pyrite precipitation was induced by injection of $FeCl_2$ solutions, gold dissolved concentrations dropped by a factor of 5–10 (depending on the experiment), in response to the large decrease of aqueous S concentration upon scavenging by pyrite and the resulting breakdown of gold-sulfur complexes. The Au aqueous concentrations after pyrite precipitation either increase by a small factor (2–3) with time (e.g., CoPy1), remain stable (CoPy2), or slightly decrease (CoPy3), likely reflecting the longer times for the system to recover after a large and rapid change in S concentration, and the different reaction kinetics of Au-pyrite-fluid exchange and pyrite recrystallization, which may depend on fluid composition, acidity, and temperature.

The concentrations of other fluid constituents (total S, K, Cl) are in excellent agreement with the initial and injected quantities. Measured total dissolved sulfur contents (S_{tot}) are identical within errors to the sum of aqueous sulfide and sulfate concentrations in CoPy2 and CoPy3, suggesting that other S species concentrations (e.g., radical ions, polysulfides) are small. By contrast, in more acidic CoPy1 experiment, S_{tot} concentrations are by 20–30% higher than the sum of sulfate and sulfide, likely due to the presence of molecular sulfur in the experiment, as demonstrated by in situ Raman spectroscopy on similar solutions (Pokrovski and Dubessy, 2015); this form of sulfur is not analyzable in sampled fluids by the I_2, CdS and $BaSO_4$ protocols employed in this study (Section 2.4). A more detailed account of sulfur speciation and isotope fractionation in these experiments will be given elsewhere.

3.1.3. Comparison of Au solubility between the two methods

The dissolved Au concentrations in the flexible-cell reactor experiment at 450 °C and 700 bar (CoPy3, Table 2) before and after HCl injection can directly be compared with those from batch-reactor runs of similar *P-T* and fluid composition (Py4 and 5; Table 1), in particular to evaluate the accuracy of the batch-reactor solubility measurements. The Au concentrations measured in batch reactors both in alkaline and neutral solutions (~2800 ppm Au in Py5, 0.5 m $K_2S_2O_3$-0.3 m KOH; ~1600 ppm Au in Py4, 0.5 m $K_2S_2O_3$; Table 1) are 2–3 times higher than the flexible-cell reactor Au concentrations at similar solution compositions (~1300 ppm Au in CoPy3, initial fluid with 0.5 m $K_2S_2O_3$-0.3 m KOH; ~600 ppm Au in fluid after HCl injection resulting in almost complete neutralization of KOH, ~0.41 m $K_2S_2O_3$-0.2 m KCl). Such discrepancies cannot be caused by minor differences in solution composition between the two types of dissolution experiments or by the presence of pyrite in the batch-reactor experiments since pyrite solubility is negligibly small at these conditions as shown by thermodynamic modeling (< 10^{-4} m Fe). Therefore, the overestimated Au concentrations in the S-rich solutions in the batch-reactor compared to the flexible-cell reactor experiments at 450 °C are likely due to enhanced dissolution of Au during the temperature rise in batch-reactor runs that largely exceeds the Au saturation concentrations at 450 °C. Indeed, thermodynamic predictions of gold solubility, using the stability constant for the dominant $Au(HS)_2^-$ complex at this pH range (see Section 2.8), show a solubility maximum at 200–250 °C in neutral-to-alkaline S-rich solutions, followed by a pronounced solubility decrease at higher *T*, with Au saturation concentrations ~10 times lower at 450 °C (Fig. A2a,b). Such Au solubility pattern versus temperature in sulfide solutions is known for a long time (Pokrovski et al., 2014; references therein). Considering the very fast dissolution kinetics of metallic Au in such solutions over the *T* range 150–450 °C, as was shown by time-dependent in-situ XAS measurements (Pokrovski et al., 2009a), it is thus very likely that some additional Au was added to the solution by dissolution between ~200 and ~300 °C during heating of the batch reactors. When reaching 450 °C, such Au-rich solution became oversaturated and gold re-precipitated on the reactor walls, contributing both to the washout solution and weight loss analyses reported in

Table 4
Adopted gold solubility and speciation in equilibrium with metallic gold and pyrite in S-rich hydrothermal fluid, and pyrite/fluid partition coefficient for chemically bound Au(I), obtained in this study from pyrite-fluid exchange and Au-pyrite co-precipitation experiments.

Run	Adopted Au solubility in fluid in equilibrium with gold metal and pyrite, ppm	Calculated fluid pH	Dominant Au(I) aqueous species in fluid	Au(I) chemically bound in pyrite, ppm	Partition coefficient $D_{py/fl}$ (Au(I))[a]
Pyrite-gold exchange experiments, 450 °C, 700 bar					
Py1	150	4.4	$Au(HS)S_3^-$	50	0.33
Py2	440	5.4	$Au(HS)S_3^-$	58	0.13
Py3	237	5.4	$Au(HS)S_3^-$	42	0.18
Py4	832	6.6	$Au(HS)S_3^-$ + $Au(HS)_2^-$	141	0.17
Py5	1394	8.0	$Au(HS)_2^-$ + Au-S_2^- + other complexes	204	0.15
Po1	426	5.8	$Au(HS)S_3^-$	54	0.13
Po2	946	8.1	$Au(HS)_2^-$ + Au-S_2^- + other complexes	116	0.12
Pyrite-gold co-precipitation experiment, 450 °C, 700 bar					
CoPy3	91	6.6	$Au(HS)_2^-$ + $Au(HS)S_3^-$	< 390[a]	< 4.2[b]
Pyrite-gold co-precipitation experiments, 350 °C, 400 bar					
CoPy1	37	4.5	$Au(HS)S_3^-$	1664	45.0
CoPy2	51	7.4	$Au(HS)_2^-$	636	12.5
Error	± 20%	± 0.2 unit		± 25%	± 30%

[a] Equation (4).
[b] Maximum value, since Au(I) in pyrite was below detection limit in this experiment.

Table 1. This artifact of the batch-reactor method, which has not been recognized in previous studies that employed the same technique in S-rich (> 0.5 m) neutral to alkaline solutions (e.g., Trigub et al., 2017b), requires corrections when interpreting Au speciation and solubility.

Consequently, in the following discussion (Section 4.1), we tentatively corrected by a factor of 0.5 the measured Au concentrations in batch-reactor runs Py4 and Py5. By contrast, in more acidic S-rich solutions, in which Au speciation is dominated by $Au(HS)S_3^-$, gold solubility only weakly depends on temperature, and thus is not expected to be overestimated in batch-reactor experiments (Fig. A2c). Similarly, at lower sulfide concentrations (< 0.2 m, such as in Po1 and Po2 runs, in which > half of initial S was consumed by pyrite formation), the amplitude of Au solubility decrease from 250 to 450 °C is much smaller and thus may be neglected. The Au aqueous concentrations adopted in this study are reported in Table 4 and used for interpreting Au aqueous speciation and fluid-pyrite partitioning (Sections 4.1 and 4.3).

3.2. Gold state and concentration in pyrite from conventional analyses

The complementary analytical methods employed in this study help distinguish the different states of gold associated with pyrite and estimate their approximate concentrations in the solid phase (Table 3). Visible gold contents in pyrites from exchange experiments determined by SEM mapping are highly variable, ranging from ~100 ppm for runs starting with pyrite (Py1–5) to ~20,000 ppm in runs starting with FeS (Po1 and 2). The Au enrichment in the Po runs is due to precipitation of native gold from the solution upon sulfidation of FeS to FeS_2 and scavenging of part of sulfur from the fluid and the resulting decrease in gold solubility, as a result of fast gold-fluid re-equilibration (Section 3.1). Native gold contents estimated by SEM, despite their large uncertainties (> 50% of the value, Section 2.2), compare reasonably well with total Au contents in the solid phase determined by aqua-regia digestion followed by ICP-AES. These contents are 100 s ppm for Py runs and 1000 s ppm for Po runs. Furthermore, an independent estimate of the total gold amount associated with pyrite in batch-reactor experiments may be made from the difference between Au concentrations in the fluid phase derived from analyses of washout solutions and those calculated from weight loss of the Au foil using the same mass of fluid (Table 1). For the Py runs this difference is zero within errors (with a single expection of Py2 run). In contrast, in the two Po runs Au weight-loss significantly exceeds Au washout solution content; this difference corresponds to pyrite-scavenged Au concentrations of ~10,000 ppm, fairly comparable (within 50%) with those derived from SEM and total digestion analyses (Table 3).

An attempt to determine invisible gold contents in pyrites was made using EPMA by carefully avoiding microscopic grains of native gold. These contents were found to be only slightly higher (factor of < 2) than the detection limit of the technique (< 120 ppm Au) for all pyrites from exchange experiments, and thus EPMA analyses may provide only qualitative information. Nevertheless, the variation of Au concentrations among different data points acquired at different positions at the grain and for different grain sizes (from 5 to ~50 μm) is rather small (relative standard deviation, RSD < 20%, Table 3), suggesting no significant invisible gold zoning or noticeable enrichment of small grains. In contrast, pyrites from co-precipitation runs (Copy1 and 2) exhibit quantifiable invisible Au concentrations of 1000 s ppm on average but with significant data scatter (RSD > 50%, Table 3) likely due to presence of heterogeneously distributed submicron to nano particulate gold, which could be observed at highest magnification in the SEM-BSE images of Au-bearing precipitated pyrite (Fig. 2e, f).

LA-ICPMS analyses of selected samples also show a rather heterogeneous gold distribution across an individual pyrite grain and between different grains in the same sample (Table 3, Fig. A3). Coexistence of spiky signals and regions of relatively constant signal intensity as a function of time in the same ablation measurement confirms, in agreement with the other conventional methods above, the presence of different types of gold in pyrite at micron scale. These include relatively large (μm size) particles of native gold, together with clusters of smaller sub-micron particles, and crystal domains with more homogeneously distributed invisible gold. The few spatially resolved data points that could be acquired across rare large grains (40–50 μm) or on individual grains of different size (from 10 to 50 μm) do not show systematic correlations with Au concentration (Fig. A3). Because of the relatively low spatial resolution of LA-ICPMS, compared to SEM and EPMA, and small data statistics, no further quantification was possible for our fine grain samples. Nevertheless, despite these limitations of LA-ICPMS, the mean Au concentrations for each analyzed sample (Py2, Py5, Po1, and CoPy3; Table 3) match within errors those of invisible gold from EPMA and XAS analyses. A more accurate assessment of the different Au chemical forms and their fractions is provided by HR-XAS spectroscopy in the following section.

3.3. Gold speciation and concentration in pyrite from HR-XANES spectroscopic analyses

HR-XANES scans were recorded on relatively “flat” regions of the

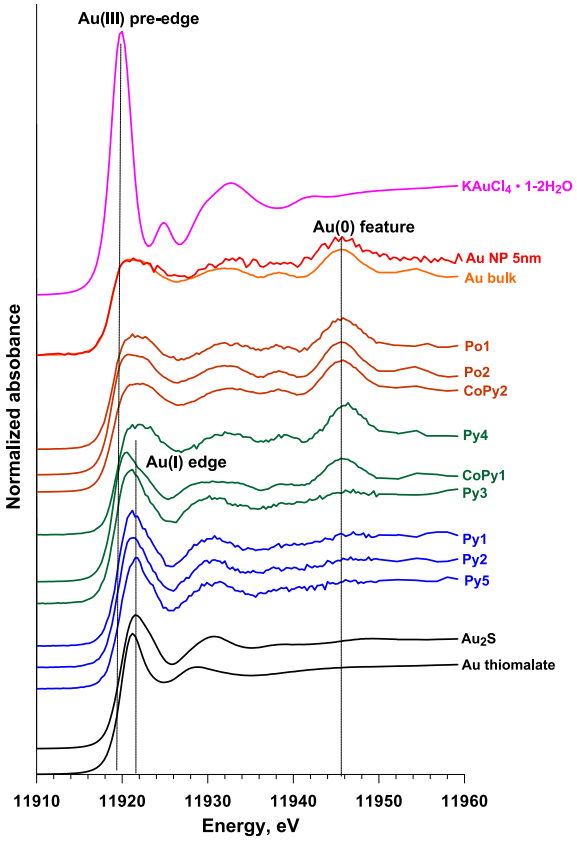

Fig. 4. Normalized Au L_3-edge HERFD XANES spectra of experimental pyrite samples and selected reference compounds. The major distinguishing features of Au(0), Au(I) and Au(III) spectra are indicated by vertical lines. Pyrite spectra are grouped according to the dominant Au state: Au(0) (Po1,2, Py4, Copy2, CoPy3 - not shown), Au(I) (Py1, 2 ,3, 5), and both Au(0) and Au(I) (CoPy1). All spectra have the same Y-axis scale, but are shifted vertically for clarity. 'Au bulk' corresponds to metallic gold of particle size ~1 μm; 'Au NP 5 nm' denotes gold nanoparticles of 5 nm diameter stabilized in phosphate saline solution.

pyrite pellets (i.e., those showing a constant fluorescence signal versus beam spot position, e.g., Fig. A1) by avoiding large Au particles (> 1 μm) clearly identifiable by their intense fluorescence signals and XANES spectra similar to those of native gold references. The total invisible Au concentration, which is determined using the edge step height of the fluorescence spectrum at each acquisition point (Eq. (2)), varied < 20% of the value; its average for each sample is reported in Table 3. These fluorescence-derived invisible gold concentration values are far more accurate than those from the EPMA and LA-ICPMS analyses above, since the technique is sensitive enough (detection limit is < 1 ppm Au) and more representative of the whole sample because of the much larger X-ray beam size (~300 μm) than the EPMA (1–3 μm) or LA-ICPMS (20–30 μm). Thus, the fluorescence-derived values of invisible gold concentration were retained in the subsequent interpretation (Section 4).

Absorption edge-height normalized XANES spectra of selected pyrite samples are shown in Fig. 4. There are three groups of samples differing by the dominant state of invisible Au, as inferred by comparisons with the spectra of metallic gold and Au(I) and Au(III) reference compounds. Some pyrites (Po1, 2; CoPy2, 3) have spectra very similar to those of elemental gold demonstrating that Au(0) largely dominates in those samples. The two major distinguishing features of the HR-XANES Au(0) spectrum are *i)* a relatively low-amplitude white-line with a wide uneven top over 11,920–11,923 eV, and *ii)* an intense resonance centered around 11,945 eV. These main features are little sensitive to gold particle size, ranging from > 1 μm down to 5 nm, as shown by XANES spectra of micron-particle Au metal and a nano-particle Au suspension (Fig. 4). The spectra directly confirm the large abundance of metallic gold in the first group of samples as also qualitatively indicated by SEM, EPMA and LA-ICPMS (Table 3). Another group of samples (Py1, 2, 3, 5) exhibits XANES spectra very different from those of Au(0) and Au(III) compounds but strikingly similar to those of Au(I) S-bearing compounds such as Au_2S, Au-thiomalate or Au-thiosulfate (not shown), as to the energy position, shape and amplitude of the white line at ~11,921 eV and the post-edge resonance at ~11,930 eV. These spectral features are characteristic of Au(I) coordinated by two sulfur atoms in a linear geometry, typical for the majority of Au(I)-S compounds (e.g., Pokrovski et al., 2009a). In addition, Py1 sample exhibits a very minor, yet detectable, Au(0) feature at 11,945 eV (which can be quantified using LCF analyses below). The third group of samples (Py3, 4; CoPy1) displays spectra with both Au(I) and Au(0) features. Note also that the spectra of all pyrite samples are clearly distinct from those of Au(III)-bearing compounds (e.g., $KAuCl_4{\cdot}2H_2O$), which show a very intense feature at 11,920 eV due to the 2p-5d transition, allowed in Au^{3+} but forbidden in Au^{+} (Berrodier et al., 2004; Pokrovski et al., 2009b), together with other smaller post-edge resonances, which are all absent in the pyrite spectra, demonstrating that no Au(III) occurs in our samples.

To further quantify the fractions of Au(0) and Au(I), linear combination fit (LCF) analyses were performed on the pyrite spectra using as reference compounds metallic Au for Au(0) and Au(I) sulfide (Au_2S), thiosulfate or thiomalate for Au(I) (Au_2S giving the best fit quality). An example of LCF is given in Fig. A4. Owing to contrasting spectral features of Au(I) and Au(0) in high-resolution mode, our method has a detection limit for Au(0) of ~3 mol% and an uncertainty of ± 3% on the value of Au(0) mole fraction, as evaluated using variable fit energy ranges and different Au(I) compounds as standards. The fraction of chemically bound Au in pyrite samples, Au(I), relative to total Au, Au (I) + Au(0), derived from LCF is reported in Table 3. These data allow direct quantification of the absolute Au(I) concentrations, which are the product of Au(I) mole fraction and the total invisible Au concentration from fluorescence spectra (as determined using Eq. (2), Section 2.6).

3.4. Gold structural position in pyrite from FDMNES-simulated XANES spectra

Comparisons of the experimental XANES spectra of Au-bearing pyrites with those of reference compounds indicate that invisible chemically bound Au associated with pyrite is likely present as S-Au(I)-S moieties (i.e., part of a molecule), probably associated with more distant atoms (Fig. 4). However, the absence of stable Au-Fe-S-bearing solids with well-known stoichiometry and structure whose spectra could be included in the comparison does not allow unambiguous assessment of other possible Au coordination environments and their contribution to the spectral signal. For example, some previous studies (e.g., Trigub et al., 2017a) suggested that chemically bound Au might also substitute for Fe or S in the pyrite structure; however, there is no unambiguous proof for such models in the absence of adequate reference compounds.

To verify the impact of such potential substitutions on the XANES signal, we simulated XANES spectra of Au in the Fe and S crystallographic sites of pyrite using the FDMNES code. The Au-Fe/S distances and site geometries ranged from those of a regular pyrite structure, in which Fe is octahedrally coordinated by 6 S atoms at 2.26 Å, and S is surrounded by 1 S and 3 Fe atoms in a distorted tetrahedron, to those of relaxed structures, in which the Fe substitution site is expanded to accommodate an AuS_6 octahedron with Au-S distances between 2.40 and 2.50 Å as predicted by Density Functional Theory (DFT) simulations (Appendix A). The resulting calculated XANES spectra were found to be only weakly sensitive to variations of Au-S and Au-Fe distances within the same coordination geometry. The main factor affecting the XANES spectral shape, white line intensity, and energy position is no doubt the Au nearest coordination sphere itself (i.e., number and cluster geometry

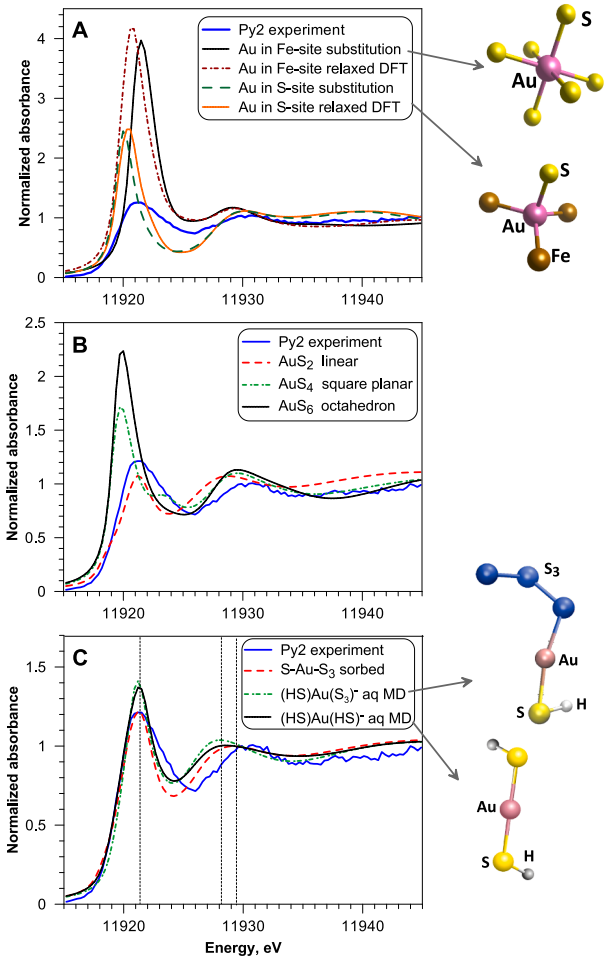

Fig. 5. Normalized Au L_3-edge HERFD XANES spectra of a representative experimental sample with dominantly chemically bound Au (Py2) and its comparison with FDMNES simulated spectra of (A) representative Au substitution models in the pyrite structure for Fe and S sites pictured by AuS_6 and $AuFe_3S$ clusters; (B) simple 2-, 4- and 6-coordinated AuS_n clusters of the indicated geometry, and (C) major Au-S aqueous complexes simulated using molecular dynamics with pictured structures of the $Au(HS)S_3^-$ and $Au(HS)_2^-$ species (from Pokrovski et al., 2015). It can be seen that none of Au substitution models in pyrite crystallographic sites (Fe and S) can account for the experimental spectra, which are best matched by S-Au(I)-S_3 clusters in which gold is linearly coordinated to 2 sulfur atoms at 2.30 Å in the nearest atomic shell. Vertical dashed lines in (C) indicate the energy shifts between the calculated spectra of different Au species (see Section 3.4 for detailed discussion).

of the first-shell neighbors). It can be seen in Fig. 5a that calculated spectra for Au in Fe and S sites in the pyrite structure are characterized by very intense white line and significant energy shifts as compared with the experimental spectrum. The differences are far too large to be attributed to imperfections of the FDMNES simulations or chosen structural models and calculation parameters.

The FDMNES parameters have been validated by simulations of spectra of reference compounds with known structures, which were found to adequately match the experimental spectra (Fig. A5) and, in particular, the white-line intensity and position which is primarily function of absorber first-shell coordination (Au site geometry and identity of neighboring atoms). The effect of coordination environment is further demonstrated by simulations of XANES spectra of isolated AuS_n clusters ($2 < n < 6$), with geometries ranging from linear AuS_2 to square-plane or tetrahedral AuS_4 to octahedral AuS_6 with Au-S distances from 2.3 to 2.5 Å. It can be seen in Fig. 5b that there is a net increase in the white-line intensity with increasing Au coordination by S from 2 to 6, with the best match of the experimental pyrite spectra by a linear S-Au-S cluster (Au-S distance 2.3 Å), which is the structural unit for Au(I) in most of its S-bearing solids and aqueous complexes (Pokrovski et al., 2009a). The simple AuS_2 cluster has a narrower white line and a first post-edge resonance maximum slightly shifted to lower energies compared to the experimental pyrite spectrum, likely due to the presence of more distant atoms in the latter. The effect of such atoms (H, S) on the XANES spectra of Au clusters may further be simulated by using the optimized geometries of the $Au(HS)_2^-$ and $Au(HS)S_3^-$ complexes obtained using first principles molecular dynamics in aqueous solution (Pokrovski et al., 2015). It can be seen in Fig. 5c that the FDMNES simulated XANES spectra of these species do provide a better match of the experimental spectrum than a simple AuS_2 cluster. Interestingly, there are small but distinctive differences in the spectra of the two aqueous Au complexes (white-line energy shift and energy and amplitude differences in the post-edge feature) suggesting that they might directly be distinguished in aqueous solution in high-resolution mode. Finally, even a better match with the experimental spectrum is obtained for an H-free S-Au-S_3 cluster that exhibits a white line amplitude almost identical to the experimental spectrum and an energy shift of the maximum of the first post-edge resonance toward that of the experiment (Fig. 5c). These similarities suggest that Au(I) might be adsorbed on pyrite surface as such or similar complexes, and thus S_3^- (and S_2^-) ions might favor gold scavenging by pyrite. More in-depth insight into the nature and structural environment of gold species on the pyrite surface requires systematic molecular dynamics simulations of the structures of adsorbed complexes, which is beyond the scope of the present study.

Note that the effect of Au coordination on the XANES spectrum is neatly emphasized in the high-resolution mode, which is necessary for unambiguously distinguishing the different Au coordination environments in sulfur-bearing systems. In summary, both experimental and FDMNES-simulated XANES spectra demonstrate that invisible Au in pyrite forms di-sulfide clusters, likely bound to more distant S atoms, and no detectable incorporation of Au occurs in Fe or S sites of the pyrite structure. The nature of this gold and its fluid-mineral partitioning are discussed in the following sections.

4. Discussion

4.1. Interpretation of gold solubility and speciation in sulfur-bearing fluids

The interpretation of Au solubility measured in our experimental sulfate-sulfide systems in terms of Au aqueous complexes is primarily based on knowledge of sulfur speciation itself, which has been a subject of recent systematic research in similar systems at elevated temperatures and pressures using in situ spectroscopic methods (Pokrovski and Dubrovinsky, 2011; Jacquemet et al., 2014; Barré et al., 2017; Pokrovski and Dubessy, 2015; Pokrovski et al., 2015). These direct spectroscopic data, combined with available thermodynamic properties of the major traditional S species such as sulfate and sulfide, generally agree that the H_2S/HS^-, S_3^- and, potentially, S_2^- ions are the major ligands for gold. Fig. 6 shows the distribution of S species calculated using the available thermodynamic data, as a function of pH (equivalent to addition of HCl or KOH) at 450 °C and 700 bar in a 0.5 m thiosulfate solution used in this study. The S_2^- ion was also included in these calculations based on the few available data points from in situ Raman spectroscopy measurements of Pokrovski and Dubessy (2015) at 450 °C in similar solutions (see Table A1 for derivation of S_2^- stability constant). It can be seen that the S species concentrations are strongly pH dependent, resulting in a strong pH control on both Au complexes distribution and overall Au solubility. In this discussion, we focus mostly on Au solubility data points obtained in this study at 450 °C that represent a dataset large enough to allow a systematic examination of the effect of pH and testing different Au speciation models. Our other experiments conducted at lower temperature and lower S dissolved

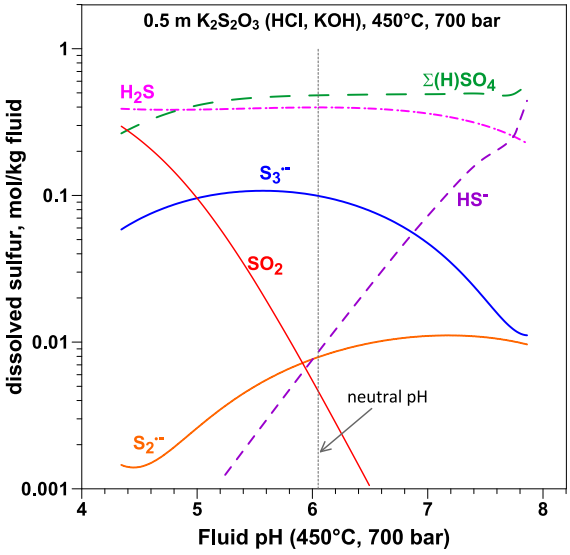

Fig. 6. Distribution of major aqueous sulfur species calculated at 450 °C and 700 bar as a function of pH (controlled by addition of HCl or KOH) in a 0.5 m $K_2S_2O_3$ aqueous solution in equilibrium with pyrite. Thermodynamic properties of the solid phases and aqueous species are from sources reported in Table A1. Concentrations of other, minor, S species such as traditional polysulfides (S_nS^{2-}), thiosulfate and other oxysulfur forms are < 0.001 m of total S at these conditions. 'Σ (H)SO_4' stands for the sum of the sulfate and hydrogensulfate ions and their ion pairs with K^+; 'HS^-' stands for the sum of HS^- ion and its KHS^0 ion pair (see Table A1 for the full list of species). The small increase of the Σ (H)SO_4 and HS^- concentrations at the most alkaline pH is due to minor breakdown of pyrite to pyrrhotite. Neutral pH value is 6.05 as defined by the dissociation constant of water ($H_2O = H^+ + OH^-$) at these *P-T* conditions (indicated by the vertical dotted line).

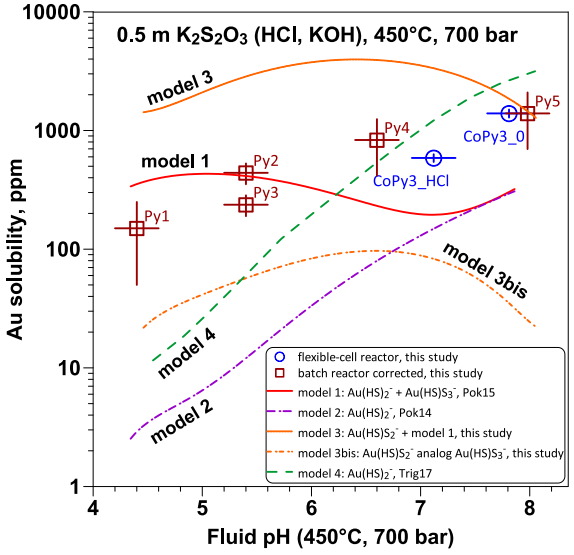

Fig. 7. Solubility of gold at 450 °C and 700 bar in a 0.5 m $K_2S_2O_3$ aqueous solution as a function of pH (controlled by addition of HCl or KOH) measured in this study in batch (Py1 to 5, squares) and flexible-cell (CoPy3, circles) reactors and its comparison with different speciation models. Model 1 (solid red curve) includes both $Au(HS)_2^-$ (Pokrovski et al., 2014) and $Au(HS)S_3^-$ (Pokrovski et al., 2015) complexes. Model 2 considers $Au(HS)_2^-$ alone from Pokrovski et al. (2014), based on experimental studies in reduced H_2S-dominated but S_3^--poor solutions. Model 3 considers in addition to the model 1 complexes, a disulfur ion complex, $Au(HS)S_2^-$, whose stability constant was adjusted to match the measured solubility at pH 8. For comparison, model 3bis shows the concentration of the same $Au(HS)S_2^-$ complex calculated assuming that the exchange reaction (3) constant between HS^- and S_2^- is equal to 1, by analogy with $Au(HS)S_3^-$ (Pokrovski et al., 2015). Model 4 considers $Au(HS)_2^-$ alone, according to recent measurements (Trigub et al., 2017a,b) in concentrated S (-NaOH) solutions using similar batch reactor technique and a simplistic S speciation model that ignores ion pairs and the sulfur radical ions and their complexes with Au.

contents (Po1 and Po2, and CoPy1 and CoPy2 runs, Tables 1 and 2) were not considered in detail here because these few data points provide insufficient pH and ligand concentration contrast in such dilute solutions to allow unambiguous discrimination among the different Au speciation models.

Fig. 7 compares the measured gold solubility at 450 °C from this study with different thermodynamic models. Model 1 includes both the $Au(HS)_2^-$ (dominant at neutral to basic pH) and $Au(HS)S_3^-$ (dominant at acidic to neutral pH) complexes, whose thermodynamic properties have been reported in recent studies based on Au solubility and in-situ XAS measurements in hydrothermal S_3^--bearing solutions (Pokrovski et al., 2015). This model predicts Au solubility in acidic conditions (pH < 6, the neutral pH at 450 °C, 700 bar being 6.05, see Fig. 6) within 50% of the experimental value, but underestimates measured solubility at neutral-to-alkaline pH by a factor of 5–10. For comparison, a traditional model involving $Au(HS)_2^-$ alone (model 2), established on a large literature dataset obtained in H_2S/HS^--dominated reducing solutions in which S_3^- is negligible (Pokrovski et al., 2014), largely underestimates, by a factor of 10–100, the measured solubility over the whole pH range; this disagreement further confirms the significance of Au-S_3^- complexes, particularly at pH < 6, but points to the existence of some additional Au species at more alkaline pH.

Because the S_2^- ion attains its maximum concentration at pH 7–8, becoming comparable with that of S_3^- (Fig. 6), an S_2^--bearing complex, $Au(HS)S_2^-$ analogous to $Au(HS)S_3^-$, was considered in an attempt to account for the measured elevated solubility in that pH range. The stability constant of $Au(HS)S_2^-$ was adjusted to match the measured solubility at pH ~ 8 at which the disagreement of experiment with both model 1 and 2 is the largest. This new model involving the three species, shown as model 3 in Fig. 7, largely overestimates the solubility at more acidic pH, clearly demonstrating that $Au(HS)S_2^-$ cannot be a dominant Au species at pH > 7. For comparison, model 3bis shows the concentration of the same $Au(HS)S_2^-$ complex calculated, following the analogy with $Au(HS)S_3^-$ (Pokrovski et al., 2015) assuming an equilibrium constant of 1 for the ligand exchange reaction

$$Au(HS)_2^- + S_2^- = Au(HS)S_2^- + HS^- \quad (3)$$

This approximation is expected to be more reasonable than model 3 above since the chemical affinities for Au(I) of the HS^-, S_3^- and S_2^- ions of same electric charge and close formal redox state of S (−1, −0.33, and −0.5, respectively) should be similar (Pokrovski et al., 2015). Thus, $Au(HS)S_2^-$ appears too weak to account for the elevated measured Au solubility at pH > 6. It cannot be excluded, however, that complexes with S_2^- ion of different stoichiometry and charge than those considered here may contribute to Au solubility the neutral-to-alkaline region, but our dataset is too small to evaluate their impact and would require more systematic work.

Finally, model 4 considers $Au(HS)_2^-$ alone, according to recent measurements of Trigub et al. (2017b) in concentrated S-NaOH solutions using a similar batch-reactor quench technique as that of our study. These authors, however, used a simplistic S speciation model compared to that in our study, by ignoring S_3^- and S_2^- ions, as well as NaHS and $Na(H)SO_4$ ion pairs and Na_2SO_4(s) precipitation in their high-temperature alkaline solutions, which all may strongly affect predictions of both pH and redox potential and the resulting Au solubility interpretation. Combined with the artifact of the batch-reactor technique leading to overestimation of Au solubility as shown in this study (Section 3.1; Fig. A1), their Au speciation model should be regarded with care. It can be seen in Fig. 7 that Trigub et al.'s model severely underestimates Au solubility at acidic pH, by at least a factor of 10, and overestimates Au solubility at neutral-to-alkaline pH by a factor of 2.

In summary, none of the models considered above can fully account for the measured Au solubility over the whole pH range at 450 °C, and in particular in the alkaline region (pH > 6), which have not been covered before by direct systematic experiments. If the actual models qualitatively agree on the existence of Au complexes with HS^-, S_3^- and, possibly, S_2^- ligands, the exact stoichiometry and charge of these complexes, in particular those with S_2^-, will require more systematic studies by both solubility and spectroscopic approaches.

4.2. The speciation of invisible gold in pyrite and comparison with literature data

4.2.1. Invisible metallic gold

Our findings of two major forms of invisible gold in pyrite, metallic gold submicron- to nanoparticles, Au(0), and chemically bound gold, Au(I), are in general agreement with the large amount of literature published over almost 50 years (e.g., Boyle, 1969; Cabri et al., 1989; Reich et al., 2005; Tauson et al., 2018; references therein). Both visible and invisible metallic gold systematically found in our experimental pyrites is likely to have precipitated *i)* on cooling and/or during the run due to minor thermal gradients favoring gold redistribution in the pyrite-fluid system (Py runs), *ii)* upon FeS_2 formation by scavenging S from solution in experiments started with FeS (Po runs), and *iii)* upon $FeCl_2$ injection inducing FeS_2 precipitation (CoPy runs), all these phenomena leading to gold-supersaturated solutions favoring metal precipitation. The degree of supersaturation, reaction time, and temperature may be the major factors controlling the size and distribution of gold particles. As it has been recognized for a long time (Kouzmanov and Pokrovski, 2012, for an overview and references therein), similar processes of fluid cooling, Fe-rich rock sulfidation, and pyrite precipitation in nature lead to formation of metal gold. Another possible process leading to nano-particle gold formation in pyrite and other sulfo-arsenides both in nature and experiment may be fluid-assisted recrystallization and breakdown of chemically bound Au that was initially incorporated into the mineral lattice or adsorbed on the surface. For example, this process likely operated in orogenic gold deposits during pyrite and arsenopyrite metamorphic recrystallization leading to expulsion of chemically bound metastable gold (e.g., Cook et al., 2009; Large et al., 2009; Velásquez et al., 2014), and in mantle chromitites hosting platinum group elements (PGE) that were subjected to fluid-assisted metamorphism leading to formation of nanoparticles of Ru-Os-Ir alloys through thermal breakdown of PGE-bearing sulfide minerals (e.g., González-Jiménez et al., 2015). In addition, slow crystal growth favoring migration and clustering of adsorbed Au complexes on the surface of arsenopyrite might be a controlling factor of nanoscale Au distribution, as recently evidenced by atom probe microscopy on arsenopyrite from the Obiasi orogenic gold deposit (Fougerouse et al., 2016). Furthermore, because solid solution miscibility is generally favored at elevated temperatures (e.g., Barton and Toulmin, 1966; Barton, 1969), cooling itself may destabilize Au dissolved as a solid solution in the mineral lattice leading to the formation of gold nanoparticles. Reheating such pyrites leads to dissolution of Au nanoparticles as was shown by in situ experiments coupled with TEM observations on Au-bearing pyrites from Carlin deposits (Reich et al., 2006). However, an opposite behavior was recently reported by Trigub et al. (2017a) who found formation of metallic gold while heating, in an anhydrous FeS_2-S system, synthetic pyrite originally containing dominantly chemically bound gold. Such behavior is at odds both with general knowledge of the thermal stability of most solid solutions and the existing in-situ observations, thus indicating that chemically bound Au in their pyrites is unlikely to be dissolved in the mineral lattice as an isomorphic substitution.

4.2.2. Redox state of chemically bound gold

If the mechanisms leading to occurrence of invisible *metallic gold* in pyrite are widely recognized and explored in existing work as outlined above, the major debate remains on the exact redox state, coordination, and structural position of *chemically bound gold*. Our data clearly demonstrate that this type of invisible Au in pyrite occurs in nominally +1 redox state (Au(I)), bound to sulfide and/or polysulfide ions, very similar to Au(I) in the fluid (such as $Au(HS)S_3^-$) and Au solids with reduced sulfur (Au_2S, Au-thiosulfate, Au-thiomalate). This finding is in agreement with some previous work using Mössbauer spectroscopy (Marion et al., 1986; Friedl et al., 1995; Palenik et al., 2004) and X-ray absorption spectroscopy on both natural (Simon et al., 1999) and synthetic (Trigub et al., 2017a) pyrites. Our results and previous data convincingly rule out the significant presence of trivalent gold, Au(III), suggested in some studies on the basis of theoretical considerations of cationic substitutions in the pyrite structure involving Fe^{2+}, Au^{3+}, As^{3+} and vacancies (e.g., Arehart et al., 1993; Chouinard et al., 2005; Deditius et al., 2008). Note that the nominally +3 redox state, Au(III), is known to only be stable in surficial oxygenated environments (e.g., Berrodier et al., 2004) or chemical compounds with strongly electronegative ligands such as F (Cotton and Wilkinson, 1988). Furthermore, trivalent gold association with reduced sulfur in pyrite would be highly unlikely because no stable Au(III) sulfide compounds are known in chemistry. Note, however, that the notion of redox state of a metal in covalent-bond dominated compounds such as those in the Au-Fe-S(-As) system should be taken with care (e.g., Cabri et al., 2000). Furthermore, in the presence of arsenic (arsenopyrite or lollingite), Au chemical state might be different and a similar debate exists on those minerals (e.g., Cathelineau et al., 1989; Genkin et al., 1998; Cabri et al., 2000), which is beyond the scope of our study that deals with As-poor systems.

4.2.3. Coordination and structural position of chemically bound gold

Another major topic of debate is Au coordination and the corresponding position in the pyrite structure. It should be emphasized that the only method enabling unambiguous determination of Au site geometry and local atomic environment is XAS. Our HR-XANES experimental spectra and FDMNES simulations collectively demonstrate that Au is coordinated in its nearest shell by two S atoms, forming [-S-Au(I)-S-] moieties, similar to those known in most Au sulfide and thiol-bearing compounds and Au-S species in hydrothermal solutions (e.g., Pokrovski et al., 2009a). Our findings agree with the pioneering XAS study of Simon et al. (1999) on pyrites from Carlin-type gold deposits. Comparisons of their XANES data with reference compounds would suggest a linear or square-planar coordination of Au with surrounding atoms, but the insufficient resolution resulting in rather featureless spectra did not allow distinguishing among the possible neighboring atoms (Fe/S/As) in that early work. The Au L_3-edge XANES spectra of experimental pyrites of our study are also similar to those of natural pyrites from orogenic gold deposits, recently investigated using high-resolution synchrotron XRF and XANES spectroscopy, showing the presence of both Au(I) and Au(0) (Stromberg et al., 2019); however, no further development concerning Au(I) structural and coordination state was given in that study. Our interpretation disagrees with a recent XAS study of Trigub et al. (2017a) who suggested, on the basis on XANES modeling and EXAFS fits of hydrothermally synthesized Au-bearing pyrites, that Au^+ substitutes for Fe^{2+} in the pyrite structure. As in our study, however, their XANES spectra astonishingly resemble those of Au_2S, and the poor signal-to-noise ratio of their pyrite EXAFS spectra renders quantification of Au coordination number and Au-ligand interatomic distances uncertain (see Appendix A for detailed comparisons). Our data clearly rule out significant Au substitution in pyrite (at least As-free), which is also in agreement with studies of Tauson's group (Tauson et al., 2018, for overview) whose early experiments showed that only a few ppm of Au could be accommodated as a solid solution in the pyrite structure in Au metal-saturated systems. These authors further suggested, based on statistical analyses of bulk Au concentration and distribution as a function of grain size of synthetic and natural pyrites, that most Au is concentrated in so called 'non-autonomous' phase forming a layer of < 1 μm thick at the pyrite surface. However,

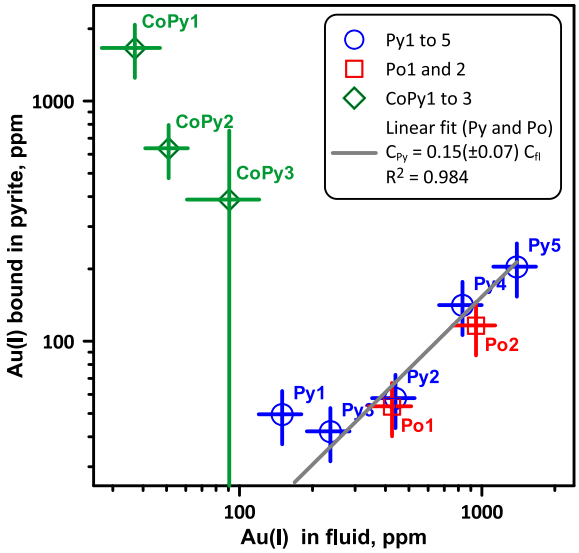

Fig. 8. Concentration of invisible chemically bound gold in pyrite as a function of equilibrium concentration of gold dissolved in the fluid phase for the three types of experiments conducted in this study (symbols). Line is a linear fit through origin (on linear scale) of the 450 °C and 700 bar data (Py and Po samples), yielding an average pyrite-fluid Au(I) partitioning coefficient ($D_{py/fl}$) of 0.15 ± 0.07. Note that D values for the two co-precipitation experiments at 350 °C (CoPy 1 and 2) are much higher ($D_{py/fl}$ between 10 and 50), while that for the 450 °C co-precipitation run (CoPy3) is ~4 ± 3 (its large uncertainty is due to the close-to-detection-limit Au(I) fraction in pyrite from this experiment).

the exact composition of such a phase and Au structural and redox state remain unknown in the absence of direct spatially-resolved spectroscopic data. Further insight into the nature of chemically bound gold in pyrite may be gained from Au pyrite/fluid partition coefficients as discussed below.

4.3. Gold partitioning between pyrite and hydrothermal fluid

The direct data obtained in this study on Au concentrations ($C_{Au(I)}$) in the fluid phase and in coexisting pyrite allow derivation of the partition coefficient of chemically bound gold between pyrite and fluid defined as

$$D_{py/fl} = C_{Au(I)}(\text{in pyrite})/C_{Au(I)}(\text{in fluid}) \quad (4)$$

A good linear correlation, apparent in Fig. 8 between Au(I) concentrations in the fluid phase and in pyrite from the exchange experiments at 450 °C and 700 bar (Py and Po runs) in a wide range of aqueous Au contents (from 10 s to 1000 s ppm), suggests an equilibrium exchange reaction. Such an exchange is little (if at all) dependent of the nature of Au(I) dominant species in the fluid ($Au(HS)S_3^-$ vs $Au(HS)_2^-$ vs $Au\text{-}S_2^-$ complexes) and the initial solid phase (pyrite vs pyrrhotite). The slope of the linear regression through zero of these data points corresponds to a partition coefficient $D_{py/fl}$ of 0.15 ± 0.07 (1 SD). The co-precipitation experiment at the same P-T conditions (CoPy3) yielded an uncertain $D_{py/fl}$ value ranging from < 0 to ~7, since Au(I) fraction in this sample dominated by metallic Au was close to the detection limit (~3 mol% Au(I), Tables 3 and 4). Considering this uncertainty, these co-precipitation data overlap, within error, with the D values from exchange experiments above. It seems thus likely that similar physical chemical processes control Au(I) partitioning into pyrite in both types of experiment. The partition coefficients of chemically bound Au for the lower-temperature co-precipitation experiments (CoPy 1 and 2 at 350 °C) are significantly higher, being of the order of 10–50 (Fig. 8, Table 4), indicating that incorporation of Au(I) in pyrite is favored at lower temperatures. This experimental finding is also in agreement with the higher abundance of chemically bound Au in pyrites from low-to-moderate temperature hydrothermal deposits (e.g., Carlin-type, epithermal) compared to pyrites from high-temperature magmatic or metamorphic deposits (porphyry, orogenic) that contain dominantly metallic gold in ore (e.g., Deditius et al., 2014; references therein).

Our Au partitioning values from pyrite-fluid exchange experiments at 450 °C are in excellent agreement with those reported by Tauson et al. (2018) from experiments at the same T and similar P ($D_{py/fl}$ = 0.3 ± 0.2). Interestingly, no effect of arsenic on Au incorporation in pyrite was found in their study at similar conditions, in agreement with the paucity of Au-rich arsenian pyrites in high-temperature hydrothermal settings. These authors interpreted such Au partitioning as an isomorphic substitution in a non-autonomous submicron-thick solid phase at the pyrite surface, but the structural and chemical position of Au in such a phase yet remain hypothetical. The methods employed in our study do not have sufficient spatial resolution to verify the existence of such a phase, which would require nano-scale in situ techniques, such as nano-beam XRD, XRF, and XAS that will potentially be offered by the next generation of synchrotrons (e.g., Dimper et al., 2014). Furthermore, the robust linear correlation between dissolved and incorporated Au(I) displayed in Fig. 8 suggests that the Au(I) activity (equivalent to concentration) in pyrite increases with increasing the activity (or concentration) of aqueous Au(I) in the fluid. Such a dependence rules out formation of Au proper solid phases (e.g., such as Au_2S) on the pyrite surface, since Au activity in such a gold-dominated phase is constant, and thus must be independent of Au activity in the fluid, which is not the case of our data shown in Fig. 8 displaying a clear positive correlation between Au in solution and pyrite. Even though our data do not rule out Au substitution as an isomorphic impurity in a non-autonomous phase suggested in Tauson's studies, a more plausible and simple explanation of the Au partitioning trends would be formation of adsorbed S-Au-S complexes on the pyrite surface, similar to those in aqueous solution as discussed below.

4.4. Chemisorption control on Au(I) incorporation in As-poor pyrite

Chemisorption has indeed been the most commonly invoked phenomenon to explain Au scavenging by (arseno)pyrite (e.g., Fleet and Mumin, 1997), but detailed physical-chemical mechanisms and driving forces of such sorption remain elusive. Only few experimental studies devoted to Au sorption on sulfide mineral surfaces are available, none of them being conducted above 90 °C, to the best of our knowledge. Some studies (Mironov et al. 1982; Bancroft and Hyland, 1990; Mycroft et al., 1995; Maddox et al. 1998; Mikhlin et al., 2011) employed acidic Au^{3+} and Au^+ chloride, cyanide, thiosulfate or citrate solutions, of little relevance to hydrothermal sulfide-bearing fluids. They found that part of Au was rapidly reduced to the metallic state on the surface of pyrite and arsenopyrite (depending of the relative stability of the Au aqueous complexes). Some other studies (Scaini et al., 1998; Widler and Seward, 2002) examined sorption by iron sulfide minerals from Au(I) sulfide solutions, but reached rather different conclusions. For example, Scaini et al. (1998) found that Au sorption on FeS_2 increased with increasing pH accompanied by Au(I) reduction to metal, whereas Widler and Seward (2002) observed a moderate decrease of $Au(HS)^0$ and $Au(HS)_2^-$ adsorption on pyrite with increasing pH above 5, with no changes in redox state of adsorbed Au(I). Furthermore, these authors found that Au(I) adsorption on marcasite and pyrrhotite was significant only in acidic solutions (pH < 4). Even though the temperature-composition parameters of our study are quite different from their work, there is a surprising similarity in acidity trends in our experiments, with the most acidic run (Py 1, pH ~ 4.4) displaying a $D_{py/fl}$ value (~0.3) twice as high as the less acidic experiments (Table 4, Fig. 8). Our values at acid pH are also close to those recently reported from fluid-pyrite Au exchange experiments in highly acidic S-H_2O solutions at 450 °C ($D_{py/fl}$ ~ 1; Trigub et al., 2017a) in line with a sorption control on Au incorporation in pyrite. Similar tendencies with pH were observed for

$Au(HS)^0$ and $Au(HS)_2^-$ sorption on As_2S_3 and Sb_2S_3 at $T < 90\,^{\circ}C$ (Renders and Seward, 1989). Because the isoelectric point of pyrite surface in H_2S-bearing aqueous solution is around pH ~ 2 at ambient conditions (i.e., pyrite surface is positively charged at pH < 2, and negatively charged at pH > 2; Bebie et al., 1998; Widler and Seward, 2002), the strong adsorption of Au-sulfide negatively charged complexes dominant in S-bearing hydrothermal fluids investigated in this study ($Au(HS)_2^-$, $Au(HS)S_3^-$) should be different from simple electrostatically controlled outer-sphere sorption of cations or anions on oxide surfaces (i.e. loose electrostatic attraction of $H_2O/H^+/OH^-$ covered surface with the absorbing ions; e.g., Dzombak and Morel, 1990). Thus, Au(I) is expected to sorb via an inner-sphere mechanism, by forming direct Au-S-Fe or Au-S_n-Fe bonds with the pyrite surface, probably similar to that of arsenite, As(III) ($As(OH)_3$ and $AsO(OH)_2^-$), sorption on FeS_2. Assuming the same surface site density for Au(I) as for As(III) (3.7 sites/nm^2; Bostick and Fendorf, 2003), it can be estimated that the maximal concentration of surface bound Au-S complexes for an ideal cubic-shape pyrite grain of 10 µm in size (having a surface area of $6 \times 10 \times 10\,\mu m^3$), representative of our experiments, would reach as much as 20,000 ppm Au if scaled to the mass of the grain. This sorption capacity is significantly superior to the Au(I) concentrations in pyrite measured in this study (< 200 ppm Au(I) at 450 °C, Table 3), thus supporting the linear trend with the concentration of Au(I) in the fluid shown in Fig. 8. Similar sorption capacities of pyrite *vis-à-vis* As(III) in aqueous solution were recently reported in siderite-to-pyrite replacement experiments at 200 °C with As contents in pyrite reaching ~10,000 ppm (Kusebauch et al., 2018), and independently by thermodynamic models of arsenian pyrite - fluid interactions at hydrothermal conditions (Xing et al., 2019). Furthermore, the plausibility of our adsorption mechanism is independently supported by natural observations of a general tendency to Au enrichment in small-grain pyrite from Carlin and MVT deposits (e.g., Reich et al., 2005; Tauson et al., 2018), since smaller grains offer larger surface areas favorable for adsorption.

Gold hydrogen sulfide and radical ions may attach to pyrite surface by forming -S-S- bonds with sulfur atoms belonging to the corners of FeS_6 octahedrons (Fig. 9). Polysulfide sulfur is ubiquitous on pyrite surfaces as systematically demonstrated by direct XPS measurements in a wide range of solution compositions at near-ambient T (e.g., Nesbitt et al., 1998; Widler and Seward, 2002; references therein) and may be a key factor for scavenging Au(I) at higher T as well, further favored by existence of direct Au complexes with poly-sulfur ions (S_3^- and S_2^-) in hydrothermal solution. The close resemblance of the XANES spectra of our Au-bearing pyrites to the simulated spectra of Au-S_3^- complexes (Fig. 5c) provides further support to this mechanism. The uptake of polysulfide Au species should also be favored during early stages of pyrite precipitation from hydrothermal fluids since pyrite formation occurs via polysulfide ion precursors (e.g., Schoonen and Barnes, 1991).

Our laboratory experiments probe the key early stages of Au incorporation in pyrite ore such as Au scavenging by preexisting pyrite and simultaneous gold-pyrite precipitation that are fast phenomena compared to natural timescales of ore deposit formation and evolution. The fate of the sorbed Au-S species during the much slower processes of further pyrite crystal growth and ageing in natural systems remains an open question in pyrite geochemistry. It is expected that some part of these sorbed Au-S clusters are incorporated in defects and dislocations of the growing crystal owing to the lack of energetically favorable crystallographic position for Au(I) in the As-free pyrite structure. Other, likely major, part of sorbed Au would be reduced into Au(0) nanoparticles that may further migrate, grow, melt or get remobilized following cooling, thermal overprint, pressure changes, and fluid-assisted metamorphism (e.g., Reich et al., 2006; Velásquez et al., 2014; González-Jiménez et al., 2015). Future improvements in sensitivity and spatial resolution of in-situ spectroscopic techniques for ppm-level metal concentrations will enable more quantitative insight into the fate of invisible gold in pyrite during such processes.

In the presence of significant amounts of arsenic in pyrite, however, the mechanisms and driving forces of Au scavenging and long-term storage may be different, since arsenic may considerably affect both surface electrical and chemical properties (e.g., Mironov et al., 1981; Möller and Kersten, 1994) and the crystal structure, for example, facilitating Au incorporation as a solid solution. Although As-bearing systems are beyond the scope of this study, our new data on fluid-pyrite partition coefficients of Au in As-poor systems indirectly support the key role of arsenic in gold enrichment in iron sulfide minerals in nature, as will be shown below.

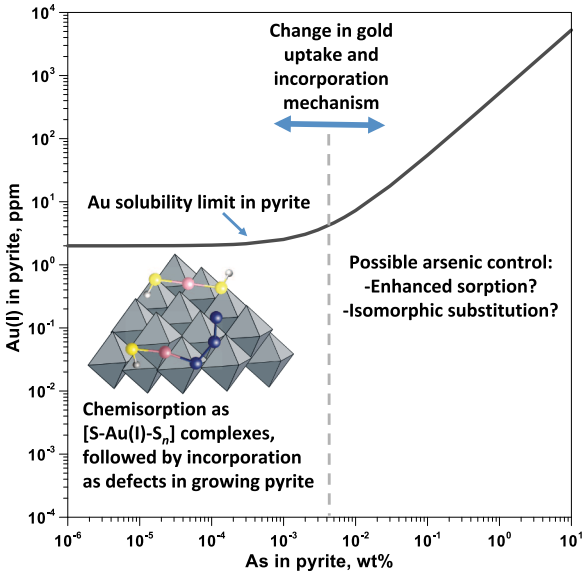

Fig. 9. Schematic diagram of gold uptake and incorporation in arsenian pyrite, as a function of arsenic content in the mineral. The dotted curve shows gold solubility limit in chemically bound state in pyrite according to Reich et al. (2005), recalculated to mass concentration units as Au(ppm) = 526 × As(wt%) + 2.0. Pyrite surface is schematically shown by FeS_6 octahedrons. Gold uptake by As-poor pyrite (< 0.01 wt% As) occurs via a chemisorption step as Au-S_n complexes similar to those in S-bearing hydrothermal fluids and their further incorporation in defects and dislocations of the growing pyrite structure. In contrast, in presence of higher As tenors in pyrite (> 0.01 wt% As), there is likely a significant change in Au incorporation control due to arsenic, leading to large enhancement of Au chemisorption and/or isomorphic substitution in the arsenian pyrite structure.

4.5. Role of arsenic in gold incorporation in pyrite

The partition coefficients of Au(I) obtained in this study allow prediction of Au dissolved contents in As-poor pyrite in nature. Detailed Au-As systematics of pyrites from various gold deposits (Carlin, orogenic, porphyry, epithermal, OICG, VHMS, and Witwatersrand) has recently been provided by Deditius et al. (2014). Their analysis demonstrates that invisible Au and As are generally positively correlated in pyrite at As contents above 0.01–0.1 wt% and that the solubility limit of chemically bound Au in arsenian pyrite is defined by an Au/As atomic ratio of 0.02 independently of the geochemical environment. Both Au and As tenors in natural pyrite generally increase with decreasing T in the range 500–200 °C.

These natural observations are in excellent agreement with our experimental data showing Au(I) pyrite-fluid partition coefficients at 350 °C ($D_{py/fl}$ ~ 10–50) significantly greater than at 450 °C ($D_{py/fl}$ ~ 0.2). Gold concentrations in hydrothermal fluids forming porphyry-epithermal and orogenic deposits, as inferred from both direct fluid inclusion analyses and thermodynamic calculations of gold solubility, are typically < 1 ppm, even though some high-temperature sulfur-rich magmatic fluids (≥ 450 °C) may exceptionally contain up to 30 ppm Au (e.g., Kouzmanov and Pokrovski, 2012; Garofalo et al.,

2014; Pokrovski et al., 2014). Combining these natural concentrations with the $D_{py/fl}$ values derived in this study at 450 °C yields Au(I) tenors in pyrite of < 3 ppm Au in high-temperature porphyry and orogenic environments. This is in agreement with the low Au(I) tenors in As-poor pyrites from such settings, which are largely dominated by metallic gold in pyrite ore. For lower temperature epithermal, Carlin, volcanic massive sulfide (VMS), and some orogenic deposits (≤350 °C) that often lack analyzable fluid inclusions, there is virtually no direct data on Au fluid contents; nevertheless, Au fluid-phase concentrations are expected to be even smaller (< 0.1 ppm Au) due to the much lower sulfide mineral solubility (pyrite and pyrrhotite) and the resulting low concentrations of reduced sulfur aqueous species (H_2S/HS^-, S_3^-), which are the key ligands for Au transport as shown in this study and previous work (e.g., Kouzmanov and Pokrovski, 2012; Pokrovski et al., 2015; references therein). Such sub-ppm Au(I) fluid concentrations, combined with our $D_{py/fl}$ values obtained at 350 °C (~10–50), would correspond to pyrite Au(I) contents of less than a few ppm. These predicted Au concentrations are in excellent agreement with the solubility limit of chemically bound gold in *arsenic-free pyrite* of 2 ppm Au (Reich et al., 2005). By contrast, our predicted values are 1 to 3 orders of magnitude lower, on average, than the Au concentrations analyzed in natural *arsenian pyrites* (> 0.01–0.1 wt% As) from these environments (Deditius et al., 2014; references therein).

Therefore, our experimental data obtained in As-free systems indirectly support the key role of arsenic in gold enrichment in arsenian pyrites and arsenopyrites from such deposits. Our results provide a sound physical-chemical interpretation of the famous wedge-shaped pattern of Au solubility in arsenian pyrite, established in the seminal work of Reich et al. (2005) on the basis of pyrite analyses from Carlin-type deposits, and more recently shown to be applicable to other types of Au deposits. According to Reich et al.'s gold solubility model in pyrite, at low As contents relevant to our study, Au(I) solubility is low (< 2 ppm) and independent of As pyrite content up to ~0.01 wt% As, but increases proportionally to As at higher As contents (Fig. 9). Our direct partitioning and spectroscopic data are in quantitative agreement with the lower-As part of the solubility curve where Au(I) incorporation in pyrite is controlled by chemisorption as Au-(poly)sulfide complexes, partly incorporated in defects and dislocations by the growing pyrite crystal, and partly rejected from the structure by reduction to Au(0) during further pyrite life. In contrast, for As-richer pyrites our data imply a fundamental change in the mechanism of Au scavenging by the mineral. Arsenic would presumably favor both chemisorption and incorporation of gold into the crystal structure as isomorphic constituent, but the physical-chemical mechanisms and driving forces of this 'arsenic effect' and Au exact structural position yet remain to be fully understood and quantified via integrated experimental, spectroscopic, and modeling studies.

5. Concluding remarks

The key points of this study are the following:

A combination of experimental, analytical and modeling approaches used in this work enables new insight into one of the oldest enigmas of Ore Deposit Research, the nature of invisible gold in pyrite. We show that gold is incorporated from hydrothermal fluids into As-poor pyrite both as native metal, Au(0) in the form of nano- and submicron particles, and as chemically bound gold of a nominal redox state of +1, Au(I).

High-resolution XANES experimental and simulated spectra of Au-bearing pyrites demonstrate that Au(I) is coordinated with two nearest sulfur atoms in a linear geometry, similar to Au(I) complexes with the HS^- and S_3^- ligands dominant in hydrothermal ore-forming fluids. The Au(I) incorporation in pyrite at molecular level is likely to proceed via specific sorption of S-Au-S aqueous species on the pyrite surface with formation of polysulfide moieties, [-S-Au-S-(S-)$_n$]. Our results rule out, at least in As-poor systems, the commonly accepted paradigm postulating Au^+ substitution for Fe^{2+} in the pyrite structure with formation of a solid solution as the mode of chemically bound Au incorporation in pyrite.

Combining the derived Au(I) content in pyrite with accurate Au concentration measurements in the coexisting hydrothermal fluid from our experiments allows generation of a first set of Au(I) partition coefficients between fluid and pyrite at *P-T* conditions typical of many types of gold deposits. These coefficients imply relatively low dissolved gold contents, of less than a few ppm Au, in As-poor pyrites (< 0.01 wt % As), in full agreement with numerous natural observations. Our estimations contrast with the elevated invisible Au contents, of 100 to 1000 s ppm Au, commonly recorded in As-rich pyrites (> 1 wt% As) and arsenopyrites (10 s wt% As) in many ore deposits; they thus highlight the fundamental control of As on Au incorporation in these minerals. Quantitative assessment of the true role of arsenic in the gold fate in fluid-mineral systems could only be achieved using a combination of cutting-edge experimental, spectroscopic and modeling approaches.

Furthermore, the results of this study highlight limitations of the existing thermodynamic and speciation models of Au in S-bearing hydrothermal fluids that still persist despite > 50 years of extensive research. In addition to 'traditional' Au complexes with HS^- ligands, our data confirm the existence, in high-temperature fluids (≥450 °C), of Au species with other ligands such as S_3^- and S_2^- ions whose nature, stability, and role in Au transport and scavenging by sulfide minerals will require future integrated research.

Acknowledgments

This work was funded by the French National Research Agency (grants RadicalS – ANR-16-CE31-0017 and SOUMET – ANR-2011-Blanc SIMI 5-6 009), the Institut des Sciences de l'Univers of the Centre National de la Recherche Scientifique (grants OrPy-CESSUR and AsOrPy-CESSUR), and the Institut Carnot ISIFoR (grant OrPet). We acknowledge the European Synchrotron Radiation Facility (ESRF) for providing access to beamtime and infrastructure. DFT calculations were performed using HPC resources from CALMIP (grant 2018-P1037). We thank P. Gisquet, A. Castillo, S. Mounic, P. Besson, C. Causserand, A. Marquet, C. Duquenoy, F. Candaudap, J. Chmelef, M. Henry, L. Menjot, J.-F. Ména, F. de Parseval, C. Laskar, A. Colin, I. Kieffer, E. Lahera, W. Del Net for their professional help with the tough hydrothermal experiments, exhausting synchrotron measurements, and tedious sample preparations and chemical analyses. We are grateful to A.-M. Cousin for the help with figure preparation. Special thanks go to Y. Joly for advice on XANES spectra modeling and to Y. Shvarov for guidance with thermodynamic calculations. We thank Editors H. Chen and C. Ciobanu for handling this manuscript and reviewers M Reich, P. Garofalo, and an anonymous referee for their insightful comments that greatly improved this article.

Appendix A. Supplementary data

Supplementary data to this article can be found online at https://doi.org/10.1016/j.oregeorev.2019.04.024.

References

Adams, M.D., ed., 2005. Advances in Gold Ore Processing. Elsevier.
Akinfiev, N.N., Diamond, L.W., 2003. Thermodynamic description of aqueous nonelectrolytes at infinite dilution over a wide range of state parameters. Geochim. Cosmochim. Acta 67, 613–627.
Amestoy, P.R., Guermouche, A., L'Excellent, J.-Y., Pralet, S., 2006. Hybrid scheduling for the parallel solution of linear systems. Parallel Comput. 32 (2), 136–156.
Arehart, G.B., Chryssoulis, S.L., Kesler, S.E., 1993. Gold and arsenic in iron sulfides from sediment-hosted disseminated gold deposits: implication for depositional processes. Econ. Geol. 88, 171–185.
Bancroft, G.M., Hyland, M.M., 1990. Spectroscopic studies of adsorption/reduction

reactions of aqueous metal complexes on sulphide surfaces. Rev. Miner. Geochem. 23, 511–558.
Barré, G., Truche, L., Bazarkina, E.F., Michels, R., Dubessy, J., 2017. First evidence of the trisulfur radical ion S_3^- and other sulfur polymers in natural fluid inclusions. Chem. Geol. 462, 1–14.
Barton Jr., P.B., 1969. Thermochemical study of the system Fe-As-S. Geochim. Cosmochim. Acta 33, 841–857.
Barton Jr., P.B., Toulmin III, P., 1966. Phase relations involving sphalerite in the Fe-Zn-S system. Econ. Geol. 61, 815–849.
Bebie, J., Schoonen, M.A.A., Fuhrmann, M., Strongin, D.R., 1998. Surface charge development on transition metal sulfides: an electrokinetic study. Geochim. Cosmochim. Acta 62, 633–642.
Berrodier, I., Farges, F., Benedetti, M., Winterer, M., Brown Jr., G.E., Deveughèle, M., 2004. Adsorption mechanisms of trivalent gold on iron- and aluminum-(oxy)hydroxides. Part 1: X-ray absorption and raman scattering spectroscopic studies of Au(III) adsorbed on ferrihydrite, goethite, and boehmite. Geochim. Cosmochim. Acta 68, 3019–3042.
Boiron, M.C., Cathelineau, M., Trescases, J.J., 1989. Conditions of gold-bearing arsenopyrite crystallization in the Villeranges basin, Marche-Combrailles shear zone, France. A mineralogical and fluid inclusion study. Econ. Geol. 84, 1340–1362.
Bostick, B., Fendorf, S., 2003. Arsenite sorption on troilite (FeS) and pyrite (FeS_2). Geochim. Cosmochim. Acta 67, 909–921.
Boyle, R.W., 1969. Hydrothermal transport and deposition of gold. Econ. Geol. 64, 112–115.
Bunau, O., Joly, Y., 2009. Self-consistent aspects of x-ray absorption calculations. J. Phys.: Condens. Matter 21, 345501.
Cabri, L.J., Newville, M., Gordon, R.A., Crozier, E.D., Sutton, S.R., McMahon, G., Jiang, D.-T., 2000. Chemical speciation of gold in arsenopyrite. Can. Mineral. 38, 1265–1281.
Cabri, L.J., Chryssoulis, S.L., De Villiers, J.P.R., Laflamme, J.H.G., Buseck, P.R., 1989. The nature of "invisible" gold in arsenopyrite. Can. Mineral. 27, 353–362.
Cathelineau, M., Boiron, M.-C., Holliger, P., Marion, P., Denis, M., 1989. Gold in arsenopyrites: crystal chemistry, location and state, physical and chemical conditions of deposition. Econ. Geol. Monograph 6, 328–341.
Cepedal, A., Fuertes-Fuente, M., Martin-Izard, A., Gonzalez-Nistal, S., Barrero, M., 2008. Gold-bearing As-rich pyrite and arsenopyrite from the El Valle gold deposit, Asturias, northwestern Spain. Can. Miner. 46, 233–247.
Chase, M.W., Jr., 1998. NIST-JANAF Thermochemical Tables, Fourth Edition. J. Phys. Chem. Ref. Data, Monograph No. 9; available at http://webbook.nist.gov/chemistry.
Chouinard, A., Paquette, J., Williams-Jones, A.E., 2005. Crystallographic controls on trace-element incorporation in auriferous pyrite from the Pascua epithermal high-sulfidation deposit, Chile-Argentina. Can. Min. 43, 951–963.
Cook, N.J., Chryssoulis, S.L., 1990. Concentrations of «invisible» gold in the common sulfides. Can. Mineral. 28, 1–16.
Cook, N.J., Ciobanu, C.L., Mao, J., 2009. Textural control on gold distribution in As-free pyrite from the Dongping, Huangtuliang and Hougou gold deposits, North China craton (Hebei Province, China). Chem. Geol. 264, 101–121.
Cotton, A.F., Wilkinson, G., 1988. Advanced Inorganic Chemistry, Fifth Edition. Wiley.
Curis, E., Osán, J., Falkenberg, G., Bénazeth, S., Török, S., 2005. Simulating systematic errors in X-ray absorption spectroscopy experiments: Sample and beam effects. Spectrochim. Acta B 60, 841–849.
Deditius, A.P., Utsunomiya, S., Renock, D., Ewing, R.C., Ramana, C.V., Becker, U., Kesler, S.E., 2008. A proposed new type of arsenian pyrite: composition, nanostructure and geological significance. Geochim. Cosmochim. Acta 72, 2919–2933.
Deditius, A.P., Utsunomiya, S., Reich, M., Kesler, S.E., Ewing, R.C., Hough, R., Walshe, J., 2011. Trace metal nanoparticles in pyrite. Ore Geol. Rev. 42, 32–46.
Deditius, A.P., Reich, M., Kesler, S.E., Utsunomiya, S., Walshe, J., Chryssoulis, S.L., Ewing, R.C., 2014. The coupled geochemistry of Au and As in pyrite from hydrothermal deposits. Geochim. Cosmochim. Acta 140, 644–670.
Den Besten, J., Jamieson, D.N., Ryan, C.G., 1999. Lattice location of gold in natural pyrite crystals. Nucl. Instrum. Meth. B 152, 135–144.
Dimper, R., Reichert, H., Raimondi, P., Ortiz, L.S., Sette, F., Susini, J., 2014. ESRF Upgrade Program Phase II (2015–2022). The Orange Book, ESRF http://www.esrf.eu/Apache_files/Upgrade/ESRF-orange-book.pdf.
Driesner, T., Heinrich, C.A., 2007. The system H_2O–NaCl. Part I: correlation formulae for phase relations in temperature–pressure–composition space from 0 to 1000 °C, 0 to 5000 bar, and 0 to 1 XNaCl: Geochim. Cosmochim. Acta 71, 4880–4901.
Dzombak, D.A., Morel, F.M.M., 1990. Surface Complexation Modeling: Hydrous Ferric Oxide. Wiley.
Fleet, M.E., Mumin, A.H., 1997. Gold-bearing arsenian pyrite and marcasite and arsenopyrite from Carlin Trend gold deposits and laboratory synthesis. Am. Mineral. 82, 182–193.
Fougerouse, D., Reddy, S.M., Saxey, D.W., Rickard, W.D.A., van Riessen, A., Micklethwaite, S., 2016. Nanoscale gold clusters in arsenopyrite controlled by growth rate not concentration: evidence from atom probe microscopy. Amer. Miner. 101, 1916–1919.
Friedl, J., Wagner, F.E., Wang, N., 1995. On the chemical state of combined gold in sulfidic ores: conclusions from Mössbauer source experiments. Neues Jahrb. Mineral. Abh. 169, 279–290.
Garofalo, P.S., Fricker, M.B., Günther, D., Barsani, D., Lottici, P.P., 2014. Physical-chemical properties and metal budget of Au-transporting hydrothermal fluids in orogenic deposits. Geol. Soc. London Spec. Publ. 402, 71–102.
Genkin, A.D., Bortinikov, N.S., Cabri, L.J., Wagner, F.E., Stanley, C.J., Safonov, Y.G., McMahon, G., Friedl, J., Kerzin, A.L., Gamyanin, G.N., 1998. A multidisciplinary study of invisible gold in arsenopyrite from four mesothermal gold deposits in Siberia, Russian Federation. Econ. Geol. 93, 463–487.
Goldschmidt, V.M., 1937. The principles of distribution of chemical elements in minerals and rocks. The seventh Hugo Müller lecture, delivered before the Chemical Society on March 17th, 655–673.
González-Jiménez, J.M., Reich, M., Camprubí, A., Gervilla, F., Griffin, W.L., Colás, V., O'Reilly, S.Y., Proenza, J.A., Pearson, N.J., Centeno-García, E., 2015. Thermal metamorphism of mantle chromites and the stability of noble-metal nanoparticles. Contrib. Miner. Petrol. 170 (15), 1–20.
Guda, S.A., Guda, A.A., Soldatov, M.A., Lomachenko, K.A., Bugaev, A.L., Lamberti, C., Gawelda, W., Bressler, C., Smolentsev, G., Soldatov, A.V., Joly, Y., 2015. Optimized finite difference method for the full-potential XANES simulations. Application to molecular adsorption geometries in MOFs and metal-ligand intersystem crossing transients. J. Chem. Theory Comput. 11, 4512–4521.
Guillong, M., Meier, D. L., Allan, M. M., Heinrich, C. A., and Yardley, B. W. D., 2008. SILLS: A MATLAB-based program for the reduction of laser ablation ICP-MS data of homogeneous materials and inclusions. In: Laser Ablation ICP-MS in the Earth Sciences: Current Practices and Outstanding Issues (Sylvester P., ed.). Miner. Ass. Can. Short Course Ser. 40, 328–333.
Gundlach-Graham, A., Garofalo, P.S., Schwarz, G., Redi, D., Günther, D., 2018. High-resolution, quantitative element imaging of an upper crust, low-angle cataclasite (Zuccale fault, Northern Apennines) by laser ablation ICP time-of-flight mass spectrometry. Geostand. Geoanal. Res. 42, 559–574.
Heinrich, C.A., Eadington, P.J., 1986. Thermodynamic predictions of the hydrothermal chemistry of arsenic and their significance for the paragenetic sequence of some cassiterite-arsenopyrite-base metal sulfide deposits. Econ. Geol. 81, 511–529.
Helgeson, H.C., Kirkham, D.H., Flowers, G.C., 1981. Theoretical prediction of the thermodynamic behavior of aqueous electrolytes at high pressures and temperatures: IV. Calculation of activity coefficients, osmotic coefficients and apparent molal and relative partial molal properties to 600° C and 5 kb. Am. J. Sci. 281, 1249–1516.
Jacquemet, N., Guillaume, D., Zwick, A., Pokrovski, G.S., 2014. In situ Raman spectroscopy identification of the S_3^- ion in S-rich hydrothermal fluids from synthetic fluid inclusions. Amer. Miner. 99, 1109–1118.
Johnson, J.W., Oelkers, E.H., Helgeson, H.C., 1992. SUPCRT92: A software package for calculating the standard molal thermodynamic properties of minerals, gases, aqueous species, and reactions from 1 to 5000 bar and 0 to 1000°C. Comput. Geosci. 18, 899–947. Updated version based on a series of subsequent papers reporting HKF parameters for most ions and aqueous complexes is available on line at. http://geopig.asu.edu/index.html#.
Joly, Y., 2001. X-ray absorption near-edge structure calculations beyond the muffin tin approximation. Phys. Rev. B 63, 125120.
Joly, Y., 2018. FDMNES User's Guide. http://neel.cnrs.fr/spip.php?rubrique1007&lang=en.
Kokh, M.A., Lopez, M., Gisquet, P., Lanzanova, A., Candaudap, F., Besson, P., Pokrovski, G.S., 2016. Combined effect of carbon dioxide and sulfur on vapor-liquid partitioning of metals in hydrothermal systems. Geochim. Cosmochim. Acta 187, 311–333.
Kokh, M.A., Akinfiev, N.N., Pokrovski, G.S., Salvi, S., Guillaume, D., 2017. The role of carbon dioxide in the transport and fractionation of metals by geological fluids. Geochim. Cosmochim. Acta 197, 433–466.
Kouzmanov, K., Pokrovski, G.S., 2012. Hydrothermal controls on metal distribution in Cu (-Au-Mo) porphyry systems. Soc. Econ. Geol. Special Publ. 16 (22), 573–618.
Kusebauch, C., Oelze, M., Gleeson, S.A., 2018. Partitioning of arsenic between hydrothermal fluid and pyrite during experimental siderite replacement. Chem. Geol. 500, 136–147.
Large, R.R., Danyushevsky, L., Hollit, C., Maslennikov, V., Meffre, S., Gilbert, S., Bull, S., Scott, R., Emsbo, P., Thomas, H., Singh, B., Foster, J., 2009. Gold and trace element zonation in pyrite using a laser imaging technique: Implications for the timing of gold in orogenic and Carlin-style sediment-hosted deposits. Econ. Geol. 104, 635–668.
Le Pape, P., Blanchard, M., Juhin, A., Rueff, J.-P., Manoj, D., Morin, G., Cabaret, D., 2018. Local environment of arsenic in sulfide minerals: insights from high-resolution X-ray spectroscopies, and first-principles calculations at the As K-edge. J. Anal. At. Spectrom. 33, 2070–2082.
Llorens, I., Lahera, E., Del Net, W., Proux, O., Braillard, A., Hazemann, J.-L., Prat, A., Testemale, D., Dermigny, Q., Gelebart, F., Morand, M., Shukla, A., Bardou, N., Ulrich, O., Arnaud, S., Berar, J.-F., Boudet, N., Caillot, B., Chaurand, P., Rose, J., Doelsch, E., Martin, P., Solari, P.L., 2012. High energy resolution five-crystal spectrometer for high quality fluorescence and absorption measurements on an x-ray absorption spectroscopy beamline. Rev. Sci. Instruments 83, 063104.
Maddox, L.M., Bancroft, G.M., Scaini, M.J., Lorimer, J.W., 1998. Invisible gold: comparison of Au deposition on pyrite and arsenopyrite. Amer. Mineral. 83, 1240–1245.
Manceau, A., Merkulova, M., Murdzek, M., Batanova, V., Baran, R., Glatzel, P., Saikia, B.K., Paktunc, D., Lefticariu, L., 2018. Chemical forms of mercury in pyrite: implications for predicting mercury releases in acid mine drainage settings. Environ. Sci. Technol. 52 (18), 10286–10296.
Mao, S.H., 1991. Occurrence and distribution of invisible gold in a Carlin-type gold deposit in China. Amer. Mineral. 76, 1964–1972.
Marion, P.H., Regnard, J.-R., Wagner, F.E., 1986. Etude de l'état chimique de l'or dans les sulfures aurifers par spectroscopie Mössbauer de 197Au. Comptes Rendus Acad. Sci. (Paris) 302 (II), 571–574.
Marsden, J.O., House, C.I., 2009. The Chemistry of Gold Extraction, 2nd ed. Society for Mining, Metallurgy, and Exploration Inc.
Mikhlin, Y., Romanchenko, A., Likhatski, M., Karacharov, A., Erenburg, S., Trubina, S., 2011. Understanding the initial stages of precious metals precipitation: nanoscale metallic and sulfidic species of gold and silver on pyrite surfaces. Ore Geol. Rev. 42, 47–54.
Mironov, A.G., Zhmodik, S.M., Maksimova, E.A., 1981. An experimental investigation of the sorption of gold by pyrites with different thermoelectric properties. Geochim. Int. 18, 153–160.

Möller, P., Kersten, G., 1994. Electrochemical accumulation of visible gold on pyrite and arsenopyrite surfaces. Mineral. Deposita 29, 404–413.
Mycroft, J.R., Bancroft, G.M., McIntyre, N.S., Lorimer, J.W., 1995. Spontaneous deposition of gold on pyrite from solution containing Au(III) and Au(I) chlorides: Part I, a surface study. Geochim. Cosmochim. Acta 59, 3351–3365.
Nesbitt, H.W., Bancroft, G.M., Pratt, A.R., Scaini, M.J., 1998. Sulfur and iron surface states on fractured pyrite surfaces. Amer. Miner. 83, 1067–1076.
Oelkers, E.H., Benezeth, P., Pokrovski, G.S., 2009. Thermodynamic databases for water-rock interaction. Rev. Miner. Geochem. 70, 1–46.
Palenik, C.S., Utsunomiya, S., Reich, M., Kesler, S.E., Wang, L., Ewing, R.C., 2004. "Invisible" gold revealed: direct imaging of gold nanoparticles in a Carlin-type deposit. Am. Mineral. 89, 1359–1366.
Pokrovski, G.S., Borisova, A.Y., Harrichoury, J.-C., 2008. The effect of sulfur on vapor-liquid fractionation of metals in hydrothermal systems. Earth Planet. Sci. Lett. 266, 345–362.
Pokrovski, G.S., Dubrovinsky, L.S., 2011. The S_3^- ion is stable in geological fluids at elevated temperatures and pressures. Science 331, 1052–1054.
Pokrovski, G.S., Kara, S., Roux, J., 2002. Stability and solubility of arsenopyrite, FeAsS, in crustal fluids. Geochim. Cosmochim. Acta 66, 2361–2378.
Pokrovski, G.S., Tagirov, B.R., Schott, J., Hazemann, J.-L., Proux, O., 2009a. A new view on gold speciation in sulfur-bearing hydrothermal fluids from in-situ X-ray absorption spectroscopy and quantum-chemical modeling. Geochim Cosmochim Acta 73, 5406–5427.
Pokrovski, G.S., Tagirov, B.R., Schott, J., Bazarkina, E.F., Hazemann, J.-L., Proux, O., 2009b. An in situ X-ray absorption spectroscopy study of gold-chloride complexing in hydrothermal fluids. Chem. Geol. 259, 17–29.
Pokrovski, G.S., Akinfiev, N.N., Borisova, A.Y., Zotov, A.V., Kouzmanov, K., 2014. Gold speciation and transport in geological fluids: insights from experiments and physical-chemical modelling. Geol. Soc. Spec. Publ. London. 402, 9–70.
Pokrovski, G.S., Dubessy, J., 2015. Stability and abundance of the trisulfur radical ion S_3^- in hydrothermal fluids. Earth Planet. Sci. Lett. 411, 298–309.
Pokrovski, G.S., Kokh, M.A., Guillaume, D., Borisova, A.Y., Gisquet, P., Hazemann, J.-L., Lahera, E., Del Net, W., Proux, O., Testemale, D., Haigis, V., Jonchière, R., Seitsonen, A.P., Ferlat, G., Vuilleumier, R., Saitta, A.M., Boiron, M.-C., Dubessy, J., 2015. Sulfur radical species form gold deposits on Earth. Proc. Nat. Acad. Sci USA 112, 13484–13489.
Proux, O., Biquard, X., Lahera, E., Menthonnex, J.-J., Prat, A., Ulrich, O., Soldo, Y., Trévisson, P., Kapoujyan, G., Perroux, G., Taunier, P., Grand, D., Jeantet, P., Deleglise, M., Roux, J.-P., Hazemann, J.-L., 2005. FAME: a new beamline for X-ray absorption investigations of very diluted systems of environmental, material and biological interests. Phys. Scripta T115, 970–973.
Proux, O., Lahera, E., Del Net, W., Kieffer, I., Rovezzi, M., Testemale, D., Irar, M., Thomas, S., Aguilar-Tapia, A., Bazarkina, E.F., Prat, A., Tella, M., Auffan, M., Rose, J., Hazemann, J.-L., 2017. High energy resolution fluorescence detected X-ray absorption spectroscopy: a new powerful structural tool in environmental biogeochemistry sciences. J. Environ. Quality 46, 1146–1157.
Ravel, B., Newville, M., 2005. ATHENA, ARTEMIS, HEPHAESTUS: data analysis for X-ray absorption spectroscopy using IFEFFIT. J. Synchrotron Rad. 12, 537–541.
Reich, M., Kesler, S.E., Utsunomiya, S., Palenik, C.S., Chryssoulis, S.L., Ewing, R.C., 2005. Solubility of gold in arsenian pyrite. Geochim. Cosmochim. Acta 69, 2781–2796.
Reich, M., Utsunomiya, S., Kesler, S.E., Wang, L., Ewing, R.C., Becker, U., 2006. Thermal behavior of metal nanoparticles in geologic materials. Geology 34, 1033–1036.
Reich, M., Chryssoulis, S.L., Deditius, A., Palacios, C., Zúñiga, A., Weldt, M., Alvear, M., 2010. "Invisible" silver and gold in supergene digenite ($Cu_{1.8}S$). Geochim. Cosmochim. Acta 74, 6157–6173.
Renders, P.J., Seward, T.M., 1989. The adsorption of thio gold(I) complexes by amorphous As_2S_3 and Sb_2S_3 at 25 and 90°C. Geochim. Cosmochim. Acta 53, 255–267.
Robie, R.A., Hemingway, B.S., 1995. Thermodynamic properties of minerals and related substances at 298.15 K and 1 bar (10^5 Pascals) pressure and at higher temperatures. U.S. Geol. Survey Bull. No. 2131 461.
Scaini, M.J., Bancroft, G.M., Knipe, S.W., 1998. Reactions of aqueous Au^{1+} sulphide species with pyrite as a function of pH and temperature. Amer. Miner. 83, 316–322.
Schoonen, M.A.A., Barnes, H.L., 1991. Mechanisms of pyrite and marcasite formation from solution: III Hydrothermal processes. Geochim Cosmochim Acta 55, 3491–3504.
Shvarov, Y.V., 2008. HCh: new potentialities for the thermodynamic simulation of geochemical systems offered by Windows. Geochem. Intern. 46, 834–839.
Shvarov, Y.V., 2015. A suite of programs, OptimA, OptimB, OptimC, and OptimS, compatible with the Unitherm database, for deriving the thermodynamic properties of aqueous species from solubility, potentiometry and spectroscopy measurements. Programs are available at. Appl. Geochem. 55, 17–27. http://www.geol.msu.ru/deps/geochems/soft/index_e.html.
Simon, G., Huang, H., Penner-Hahn, J.E., Kesler, S.E., Kao, L.-S., 1999. Oxidation state of gold and arsenic in gold-bearing arsenian pyrite. Amer. Miner. 84, 1071–1079.
Stefánsson, A., Seward, T.M., 2003. Stability of chloridogold(I) complexes in aqueous solutions from 300 to 600°C and from 500 to 1800 bar. Geochim. Cosmochim. Acta 67, 4559–4576.
Stromberg, J.M., Van Loon, L.L., Gordon, R., Woll, A., Feng, R., Schumann, D., Banerjee, N.R., 2019. Applications of synchrotron X-ray techniques to orogenic gold studies; examples from the Timmins gold camp. Ore Geol. Rev. 104, 589–602.
Sverjensky, D.A., Harrison, B., Azzolini, D., 2014. Water in the deep Earth: The dielectric constant and the solubilities of quartz and corundum to 60 kb and 1200 °C. Geochim. Cosmochim. Acta 129, 125–145.
Sylvester, P.J., Cabri, L.J., Tubrett, M.N., McMahon, G., Laflamme, J.H.G., Peregoedova, A., 2005. Synthesis and evaluation of a fused pyrrhotite standard reference material for platinum group element and gold analysis by laser ablation-ICPMS. In: Törmänen, T.O., Alapieti, T.T. (Eds.), 10th International Platinum Symposium: Oulu. Geological Survey of Finland, Extended Abstracts, pp. 16–20.
Tauson, V.L., 1999. Gold solubility in the common gold-bearing minerals: experimental evaluation and application to pyrite. Eur. J. Mineral. 11, 937–947.
Tauson, V.L., Lipko, S.V., Smagunov, N.V., Kravtsova, R.G., 2018. Trace element partitioning dualism under mineral-fluid interaction: origin and geochemical significance. Minerals 8, 282.
Testemale, D., Hazemann, J.-L., Pokrovski, G.S., Roux, J., Joly, Y., Argoud, R., Geaymond, O., 2004. Structural and electronic evolution of the $As(OH)_3$ molecule in high-temperature aqueous solutions: an x-ray absorption investigation. J. Chem. Phys. 121, 8973–8982.
Trigub, A.L., Tagirov, B.R., Kvashnina, K.O., Chareev, D.A., Nickolsky, M.S., Shiryaev, A.A., Baranova, N.N., Kovalchuk, E.V., Mokhov, A.V., 2017a. X-ray spectroscopy study of the chemical state of "invisible" Au in synthetic minerals in the Fe-As-S system. Amer. Miner. 102, 1057–1065.
Trigub, A.L., Tagirov, B.R., Kvashnina, K.O., Lafuerza, S., Filimonova, O.N., Nickolsky, M.S., 2017b. Experimental determination of gold speciation in sulfide-rich hydrothermal fluids under a wide range of redox conditions. Chem. Geol. 471, 52–64.
Velásquez, G., Béziat, D., Salvi, S., Siebenaller, L., Borisova, A.Y., Pokrovski, G.S., de Parseval, P., 2014. Formation and deformation of pyrite and implications for gold mineralization at the El Callao mining district. Venezuela. Econ. Geol. 109, 457–486.
Widler, A.M., Seward, T.M., 2002. The adsorption of gold(I) hydrosulfide complexes by iron sulphide surfaces. Geochim. Cosmochim. Acta 66, 383–402.
Yang, S., Blum, N., Rahders, E., Zhang, Z., 1998. The nature of invisible gold in sulfides from the Xiangxi Au-Sb-W ore deposit in Northwestern Hunan, Peoples Republic of China. Can. Mineral. 36, 1361–1372.
Xia, F., Zhou, J., Brugger, J., Ngthai, Y., O'Neill, B., Putnis, A., Pring, A., 2009. Mechanism and kinetics of pseudomorphic mineral replacement reactions: a case study of the replacement of pentlandite by violarite. Geochim. Cosmochim. Acta 73, 1945–1969.
Xing, Y., Brugger, J., Tomkins, A., Shvarov, Y., 2019. Arsenic evolution as a tool for understanding formation of pyritic gold ores. Geology 47, 335–338.